International Geology Review
Publication details, including instructions for authors and subscription information:
http://www.informaworld.com/smpp/title~content=t902953900

Petrogenesis of I-type granitoids from the Melrose Stock, east-central Nevada

A. K. El-Shazly [a]; D. D. Sanderson [a];J. Napier [a]
[a] Geology Department, Marshall University, Huntington, WV, USA

First published on: 13 May 2010

To cite this Article El-Shazly, A. K. , Sanderson, D. D. andNapier, J.(2010) 'Petrogenesis of I-type granitoids from the Melrose Stock, east-central Nevada', International Geology Review,, First published on: 13 May 2010 (iFirst)
To link to this Article: DOI: 10.1080/00206811003755396
URL: http://dx.doi.org/10.1080/00206811003755396

International Geology Review
2010, iFirst article, 1–37

Petrogenesis of I-type granitoids from the Melrose Stock, east-central Nevada

A.K. El-Shazly*, D.D. Sanderson and J. Napier†

Geology Department, Marshall University, Huntington, WV, USA

(*Accepted 7 March 2010*)

The Melrose Stock in the Dolly Varden Mountains of east-central Nevada is one of the many Mesozoic intrusion s in the Basin and Range Province. It consists of monzonites, quartz monzonites, granodiorites, and granites sharply intruding Mississippian to Triassic units. Phenocrysts of plagioclase (An_{38}–An_{24}) with oscillatory zoning and albitic rims, hornblende ± diopside, and biotite are common. Coexisting phases include orthoclase, quartz and accessory magnetite, apatite, titanite, ilmenite, and allanite. Mineral compositions suggest that the intrusion was emplaced at ~720 ± 40°C and 1.8–2.3 kbar.

All rocks are metaluminous to slightly peraluminous, defining a calcalkalic trend in which the monzonites and syenites are shoshonitic. Rare earth element patterns indicate that all studied rock types are comagmatic. Harker plots show curvilinear trends with some kinks consistent with fractionation, and mixing/assimilation. Major-element modelling and petrographic evidence suggest three stages of fractionation/mixing: Stage 1 marked by the fractionation of diopside and plagioclase; Stage 2 by fractionation of plagioclase, hornblende ± orthoclase ± biotite, accompanied by mixing through convection; and Stage 3 by fractionation of biotite, hornblende, plagioclase, and orthoclase.

Mineralogic, petrographic, and major- and trace-element data demonstrate that all rocks are I-type granitoids, suggesting a significant mantle contribution. Spider diagrams show troughs for Ti, P, and Nb, indicating magma genesis in a subduction-zone setting. Discrimination diagrams classify all rocks as late orogenic. Magma was therefore generated from mantle metasomatized by subduction, differentiated to a monzonitic magma, and emplaced in the thinned continental crust during a period of extension late in the cycle of Elko orogeny.

Keywords: Melrose Stock; I-type granitoids; monzonites; granodiorites; granites; differentiation; thermobarometry; Elko orogeny

Introduction

Granitoids (rocks ranging in composition from diorites to granites) are the most abundant plutonic rocks in the upper continental crust, especially where it has been thickened by orogeny. Despite their relatively simple and uniform mineralogy, these magmas are produced by a variety of processes that range from partial melting of pelitic+semi-pelitic schists and gneisses in the deep continental crust to fractional crystallization of mantle-derived, hypersthene-normative basaltic magma (e.g. Chappell and White 1974; Pitcher 1993; Frost *et al.* 2001). Accordingly, geochemical analysis for major and trace elements/stable and

*Corresponding author. Email: elshazly@marshall.edu
†Current address: Marshall Miller Associates, 534 Industrial Park Road, Bluefield, VA 24605, USA.

ISSN 0020-6814 print/ISSN 1938-2839 online

DOI: 10.1080/00206811003755396
http://www.informaworld.com

radiogenic isotopes is one of the main tools used for understanding the origin of granitoids, and it has played an important role in establishing classification schemes specific to these rocks (e.g. De La Roche *et al.* 1980; Pearce *et al.* 1984; Batchelor and Bowden 1985; Frost *et al.* 2001). Because the emplacement of granitoids in the solid upper continental crust requires some thermal perturbation often associated with plate dynamics, geochemical data and classification schemes of granitoids have been used for tectonic interpretations (e.g. Pearce *et al.* 1984; Maniar and Piccoli 1989; Barbarin 1990; Pitcher 1993; Winter 2010), leading to the establishment of the locations of former continental margins (e.g. Armstrong 1988; Kistler 1990; Miller and Barton 1990), as well as identification of the conditions of magma emplacement (extensional vs. compressional) or the stage within the orogenic cycle (e.g. Batchelor and Bowden 1985; Pitcher 1993).

The Melrose Stock in the Dolly Varden Mountains of east-central Nevada is one of several Mesozoic granitoid plutons in the hinterland of the Sevier Belt in the Basin and Range Province (Figure 1). As such, its formation may have been related to the Elko, Nevadan, and/or Sevier orogenies (e.g. Condie 1989; Thorman *et al.* 1992; Levin 2003),

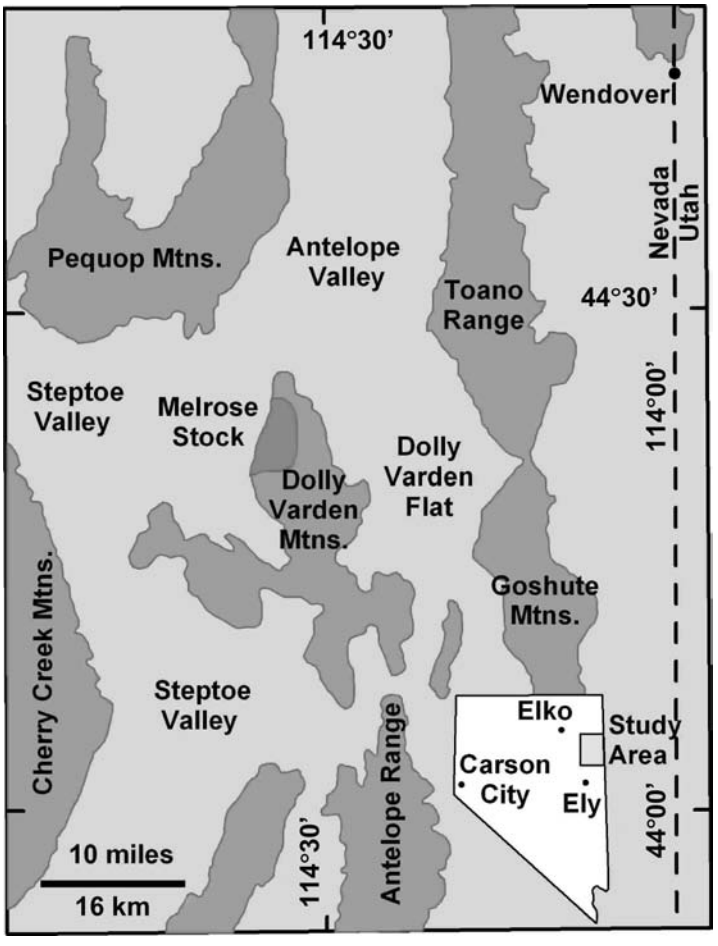

Figure 1. Map showing the location of the Dolly Varden Mountains and the Melrose Stock relative to other nearby ranges in east-central Nevada.

and was emplaced in either a compressional (syn-orogenic?) or extensional (post-orogenic?) regime. Despite its importance in understanding the tectonic evolution of the North American Cordillera, very little work has been done on this stock. Snow (1963) conducted a field study of the area and a petrological study of the stock. Sanderson's (1972) field and petrological study focused on Fe-oxides and ferromagnesian silicates of the Melrose granitoids to understand the geometric controls on their magnetic properties and using palaeo-magnetism to detect structural rotation of the stock. In a subsequent study, Sanderson (1974) suggested that the intrusion was emplaced in two phases: an earlier monzonitic magma and a later more differentiated one. Based on analysis of spatial distribution of magnetite and its association coefficient with other minerals, Sanderson (1974) concluded that the late-stage magma was emplaced more slowly and under more oxidizing conditions compared to the earlier phase of monzonite emplacement. Miller and Hoisch (1992) carried out a field and petrologic study of structures, metamorphism, and magmatism in the Pilot and Toano Ranges, northeast of the Dolly Varden Mountains. Their study led them to identify three Jurassic tectonic provinces in this part of the Basin and Range: (i) extensional in the east, (ii) modest compression in the centre, and (iii) extreme shortening to the west. Based on geographic location, Miller and Hoisch (1992) considered the Dolly Varden Mountains as part of the 'modest shortening province'.

The age of the Melrose Stock is also uncertain. Armstrong (1963) reported a K–Ar age of 125 Ma on biotite from a monzonite sample, and concluded that the stock was Early Cretaceous in age. On the other hand, the tectonic synthesis of Miller and Hoisch (1992) suggests that the stock is Jurassic, as the Dolly Varden Mountains are located within the same tectonic province that includes Jurassic plutons comprising the Pilot and Toano ranges (Figure 1). Zamudio (1993) reported a U–Pb age on zircon from the Melrose Stock of 165 Ma, supporting a Jurassic age for this intrusion.

From this summary, it is clear that the Mesozoic tectonic history of east-central Nevada is still controversial, with the debate centring on whether the structures and plutons developed in extensional or compressional regimes (e.g. Barton 1990; Elison 1991; Miller and Hoisch 1992). Understanding the petrogenesis of the different plutons in east-central Nevada is needed to refine our tectonic interpretations. Such petrogenetic interpretations are not possible without a detailed geochemical analysis. In this study, we present petrographic and geochemical data on the Melrose Stock with the aim of (1) characterizing and classifying the various rock types constituting this pluton; (2) constraining the conditions of its crystallization/emplacement; (3) understanding the petrogenesis of the various rock types constituting it and the overall evolution of the stock; and (4) constraining the tectonic settings/environments in which the magma was generated and emplaced. The results of this study may lead to a better understanding of the Mesozoic tectonic evolution of east-central Nevada, which in turn is essential for a better understanding of the North American Cordillera.

Geologic setting and field relations

The Dolly Varden Mountains are located 25 miles west of the Utah–Nevada border in southern Elko County, Nevada, where they form a northward extension of the Schell Creek and Antelope Ranges (Figure 1). The nearly N–S-trending range with an elevation of ~2000 ft is a horst within the Basin and Range Province. The Melrose Stock constitutes the core of the range, covering an area of approximately 12 square miles. The granitoid body intrudes Mississippian to Triassic limestones, dolomites, siltstones, and sandstones, best exposed along its southern margin (Figure 2). Contacts between the intrusive and the surrounding rocks are sharp, with heat-induced alteration represented by a contact metamorphic

aureole that rarely exceeds 10 ft in width (Sanderson 1972). Angular xenoliths 1–12 in long are common and increase in size and abundance towards the north-western margin of the stock. Tertiary ignimbrites and freshwater sediments overlie all units unconformably on the northern and eastern margins of the stock, whereas a normal, Basin and Range-type fault defines its western boundary, though it is covered in part by alluvium (Figure 2; Sanderson 1972).

The Melrose Stock consists of medium- to coarse-grained, commonly porphyritic granitoids, which range in composition from syenodiorites to granites. Through hand-sample and microscopic petrography, Sanderson (1972) subdivided the stock into three rock types with gradational contacts that do not allow for the unequivocal establishment of a chronological sequence of crystallization/intrusion (Figure 2). Several small dikes of medium- to fine-grained leucocratic quartz syenites cross-cut the stock.

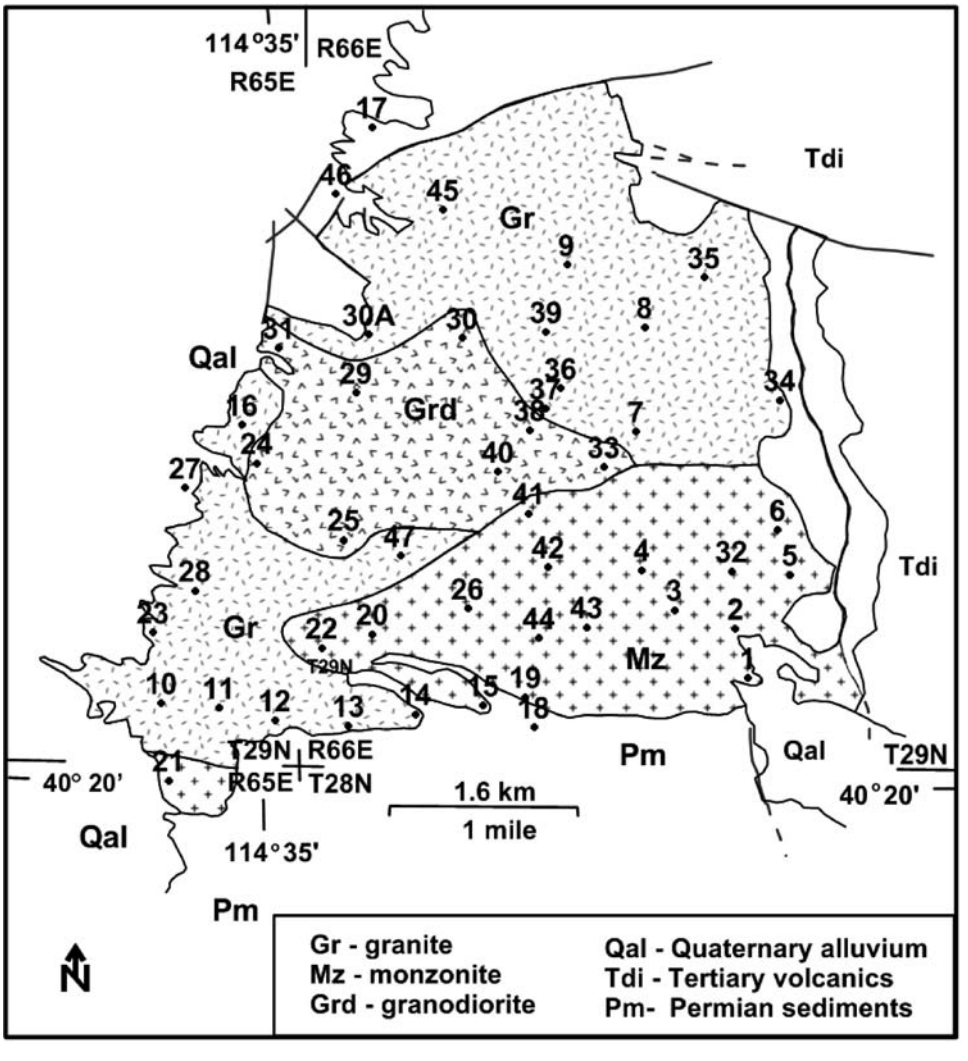

Figure 2. Simplified geological map of the Melrose Stock showing the different rock units and locations of samples studied after Sanderson (1972).

Analytical techniques

More than 50 granitoid samples were collected from 48 locations that provide a fairly uniform coverage of the Melrose Stock (Figure 2). Thin sections of these samples were examined petrographically, and their mineral modes were determined by point-counting the phases quartz, plagioclase, K-feldspar, amphibole + pyroxene, and biotite, at a magnification of 140× with a total of 1000 point counts per sample. Modal contents of pyroxene, amphibole, opaque, and other accessory phases were estimated visually. The results (partly listed in Table 1), when plotted on an International Union of Geological Sciences (IUGS) classification diagram (e.g. Le Maitre *et al.* 2002), show the samples clustering in three main groups – monzonites/quartz monzonites, granodiorites, and granites – with a few samples plotting as syenites, monzodiorites, and quartz monzodiorites (Figure 3).

Table 1. Modal contents of representative samples from the Melrose Stock.

	Pl	Kfs	Qtz	Hb	Bt	Cpx	Opq	Ttn	Others	Texture
Granites										
VN-7	40	31	22	3	5	tr	1	tr	Ap, Zrn, Aln	Porphyritic
VN-8	31	33	24	4	7	0	1	1	Ap, Zrn, Aln, Ep	Porphyritic
VN-9	27	37	25	4	5	0	1	tr	Ap, Zrn, Rt	
VN-11A	38	29	22	3	7	tr	1	1	Ap, Zrn, Chl	Porphyritic
VN-16	30	29	27	5	8	tr	1	1	Ap, Aln, Zrn, Chl	
VN-23C	32	28	28	3	8	tr	1	1	Ap, Zrn, Bsn	
VN-24	35	31	22	6	5	0	1	2	Ap, Zrn, Czo, Aln, Ms, Chl	
VN-25	39	26	23	7	5	0	2	2	Ap, Aln, Chl	
VN-30A	33	29	24	5	8	0	1	0	Ap, Zrn, Chl	Porphyritic
VN-31A	35	26	28	4	7	0	1	tr	Ap, Zrn, Aln, Chl	Porphyritic
VN-31D	45	20	26	3	5	0	1	0	Ap, Zrn, Aln, Chl	
VN-33	48	21	24	5	2	0	1	1	Ap, Rt	Porphyritic
VN-33B	32	35	21	3	7	0	1	tr	Ap	
VN-45B	39	27	22	3	7	tr	1	0	Ap	Porphyritic
VN-47A	30	26	27	5	10	0	1	0	Ap, Zrn	
Granodiorites										
VN-12B	45	19	26	3	7	0	1	1	Ap, Aln, Bsn, Chl	
VN-29	43	18	23	4	10	0	1	tr	Ap, Zrn, Aln, Chl, Ep	
VN-30	43	21	23	4	7	0	2	tr	Ap, Zrn, Aln, Chl, Cc	Porphyritic
VN-34	46	21	20	5	7	0	1	tr	Ap, Mnz, Aln, Bsn	Porphyritic
VN-40B	46	24	21	3	6	0				Porphyritic
Monzonites/Qz monzonites										
VN-2A	34	38	9	9	4	8	1	tr	Ap, Bsn, Zrn	Cumulate
VN-2B	38	36	8	15	2	0	1	tr	Ap, Bsn, Zrn	Cumulate
VN-5	32	40	9	13	5	0	1	1	Ap, Aln, Zrn, Ep, Chl	Cumulate
VN-19	32	55	4	6	3	0	1	2	Ap, Zrn, Aln, Rt	Cumulate
VN-20	35	42	2	8	6	7	1	0	Ap, Aln	Porphyritic
VN-21B	24	47	9	14	6	1	2	tr	Ap, Zrn, Bsn	Porphyritic
VN-22C	35	50	1	11	2	0	1	2	Ap, Zrn, Aln, Rt	Porphyritic
VN-22B	34	44	3	14	3	0	1	1	Ap, Zrn, Aln	Porphyritic
VN-26	35	33	1	15	13					
VN-32	31	47	5	7	6	3	1	1	Ap, Zrn, Aln	Cumulate
VN-41	43	39	4	8	2	5	2	0	Ap, Zrn, Aln, Ep	
VN-44	52	9	1	6	15	15	1	tr	Ap, Aln, Ep, Chl	Porphyritic
Syenite dike										
VN-15C	14	71	8	6	1	0	1	2	Ap, Zrn, Ep, Chl	

Notes: All abbreviations after Kretz (1983), except Opq: opaque phases, Bsn: bastnäsite-Ce.

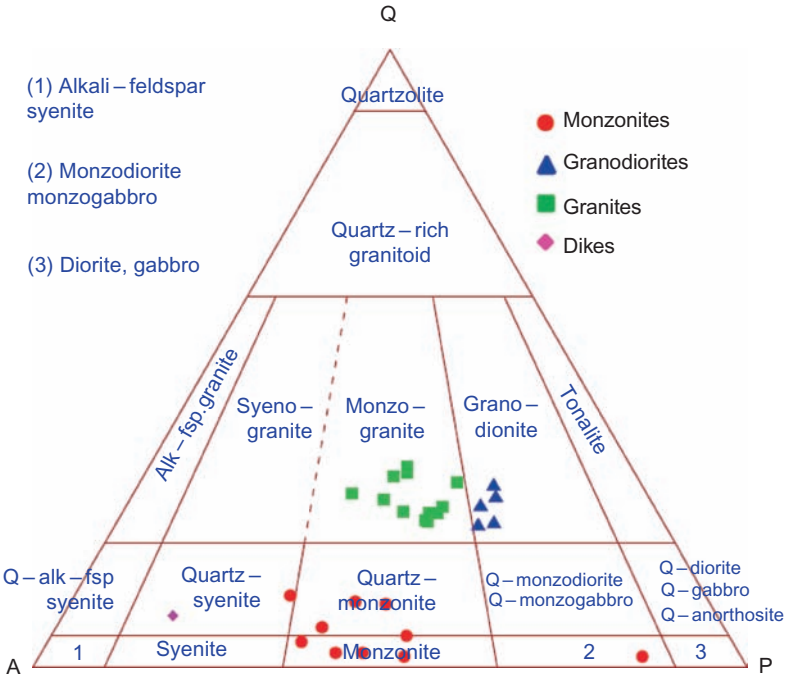

Figure 3. Modal analysis results for 27 samples plotted on the quartz–alkali feldspar–plagioclase feldspar ternary diagram following the IUGS classification (Le Maitre *et al.* 2002).

Five samples (two monzonites, one granodiorite, and two granites) were selected for microprobe work. Mineral analysis was carried out at Marshall University using a JEOL JSM-5310 LV scanning electron microscope (SEM) equipped with a Link Pentafet ultra-thin window (UTW) energy dispersive spectroscopy (EDS) detector. Analytical conditions were 20 kV operating voltage, 95 mA condenser lens current, a working distance of 20 mm, and a beam size of 2 µm. Beam current intensity was monitored on pure Co, with a calibration performed every 2 h maintaining a count rate of 26–27 kcps and a dead time of ≤25%. Standardization was performed on well-characterized Smithsonian Institution standards, all mounted on the same sample holder. Standards included microcline (Si, K, Al), scapolite (Na, Al, Cl), Kakanui hornblende (Ti), diopside (Ca, Mg), chromite (Cr), and Johnstown hypersthene (Fe, Mn). These and additional standards (e.g. Kakanui augite and Lake County plagioclase) were routinely analysed as unknowns to check on the quality of the analyses. Analytical results were processed using LINK ISIS 3.1 software and a ZAF correction. Precision is estimated at 1–2% for all oxide weight per cent values. Mineral formulae were calculated using MINFILE (Afifi and Essene 1988) or MinFormula (Tindle 2000) on the basis of 8, 6, 17, and 22 oxygens for feldspars, pyroxenes, pyriboles, and biotite, respectively. Amphibole structural formulae were calculated on the basis of 13 cations less Na, K, and Ca using AMPHIBOL (Richard and Clarke 1990).

Thirty samples representative of the different rock types were selected for whole-rock chemical analysis. The samples were pulverized in a tungsten carbide mill, and the loss on ignition was determined by heating 3 g of the powders in porcelain crucibles in a muffle furnace at 850°C for 3 h and re-weighing after cooling in a desiccator. For major-element analysis, the powders were mixed thoroughly with 1:2 lithium metaborate–lithium tetraborate flux and fused in graphite crucibles in a muffle furnace at 1000°C. The beads were then

dissolved in H_2SO_4 following the 'single-solution' method (e.g. Ingamells 1966; Suhr and Ingamells 1966; Shapiro 1975). For trace-element analysis, the powders were dissolved in polytetrafluoroethylene (PTFE) beakers with HNO_3 and HF overnight, dried, and the residue dissolved in HCl (acid digestion technique; e.g. Briggs 2002). Major- and trace-element analyses were carried out using a Liberty 110 inductively coupled plasma-atomic emission spectrometer (ICP-AES) from Varian Inc. at Marshall University, after calibration with US Geological Survey (USGS) standard GSP-1. Standards (GSP-1, AGV-1, and G-2) were routinely analysed as unknowns to check for accuracy, and appropriate correction factors were applied when necessary. Sixteen of the 30 samples analysed were selected for the analysis of trace and rare earth elements (REEs) by inductively coupled plasma-mass spectrometry (ICP-MS) at Acme Labs (Vancouver, Canada). Precision for major-element data is 1% or better (usually <0.6%), 1–2% for trace elements, and <3% for REE. Accuracy (estimated from analysing standards) is estimated at 2% or better for major elements, and 7% or better for trace elements.

Petrography and mineral chemistry

Based on Sanderson's (1972) map (Figure 2) and his modal analysis of more than 50 samples, the samples analysed in this study are classified as monzodiorites, monzonites, and quartz monzonites (herein termed collectively as 'monzonites'), granodiorites, and monzogranites (herein termed 'granites') according to the IUGS classification (Le Maitre *et al.* 2002; Figure 3; Table 3). The monzonites have 30–43% plagioclase, 9–55% K-feldspar, 1–9% quartz, 0–15% clinopyroxene, 6–15% hornblende, and 2–15% biotite, and are always characterized by hornblende + clinopyroxene > biotite. Texturally, these coarse-grained rocks are either porphyritic with phenocrysts of plagioclase ± clinopyroxene/hornblende, or cumulates with cumulus plagioclase ± clinopyroxene/hornblende and intercumulus biotite, K-feldspar, quartz, titanite ± allanite. The granodiorites contain 43–46% plagioclase, 18–24% K-feldspar, 20–25% quartz, 2–5% hornblende, and 5–10% biotite, whereas the granites contain 27–48% plagioclase, 30–35% K-feldspar, 20–28% quartz, 3–7% hornblende, 5–10% biotite, and occasional traces of clinopyroxene. Both rock types are either porphyritic with phenocrysts of plagioclase ± K-feldspar, or equigranular hypidiomorphic, but always have more biotite than hornblende. Apatite, haematite, ilmenite, and magnetite are ubiquitous, with the latter two minerals constituting 1–2% of the mode. Titanite, zircon, and allanite are very common accessory minerals, whereas rutile and epidote are rare. Secondary minerals include sericite, epidote, and calcite after feldspars, chlorite after biotite, and bastnäsite-Ce after allanite.

Feldspars

In the monzonites, plagioclase occurs as phenocrysts and finer-grained matrix crystals, or as coarse-grained cumulus crystals. Most phenocrysts have small anorthite-rich (An_{53}–An_{58}) cores, thick mantles with characteristic oscillatory zoning (typically between An_{22} and An_{38}), and significant rims of almost pure albite. Cumulus plagioclases show occasional oscillatory zoning, are characterized by thick rims of albite, or occur included in K-feldspar oikocrysts. In the granites and granodiorites, plagioclase phenocrysts (An_{18}–An_{36}; average An_{30}) have similar textures to those in the monzonites (Figures 4a and 5), but are often characterized by intermediate 'dusty/sieve-textured' zones, ~100 μm thick with abundant inclusions and significant saussuritization. In all rock types, matrix plagioclases are unzoned, sometimes displaying a myrmekitic texture along their rims.

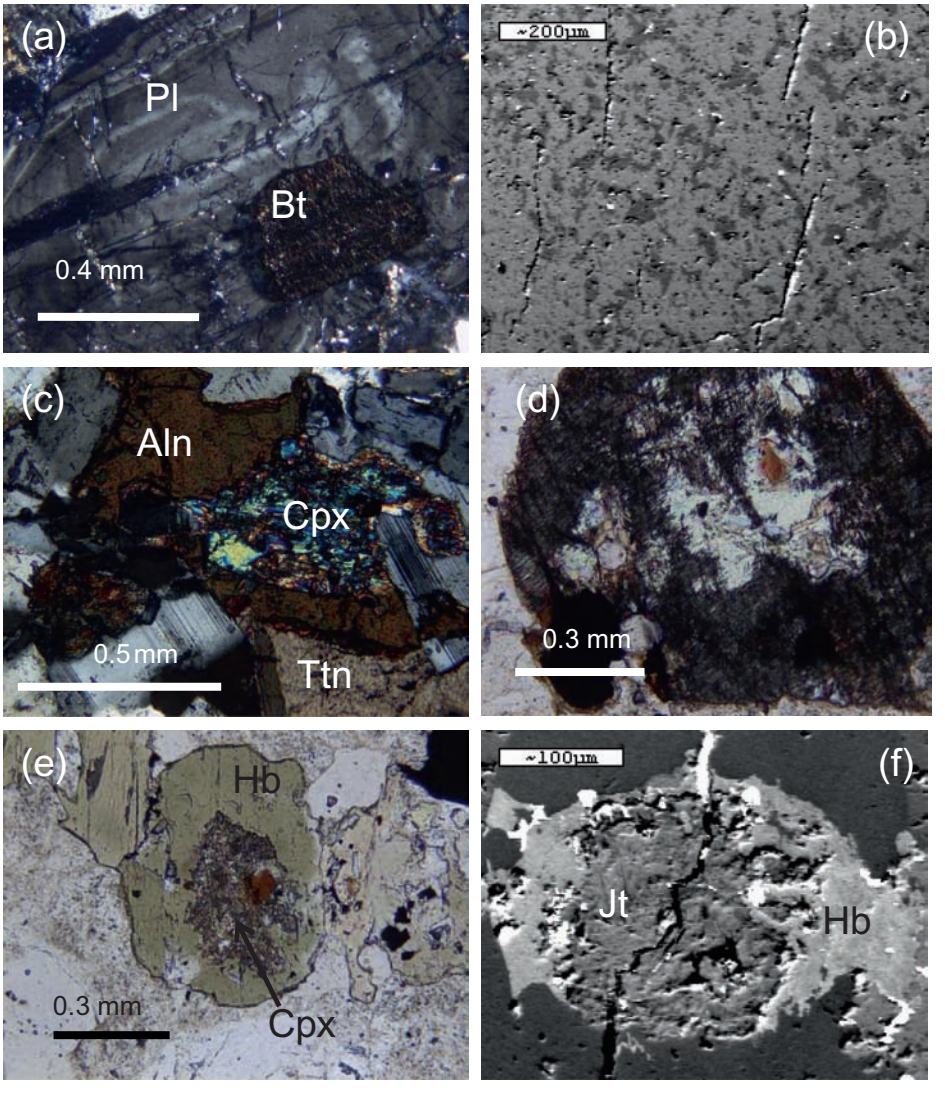

Figure 4. Selected textural relations: (a) plagioclase crystal showing oscillatory zoning, sample VN-7, crossed polarizers (Xpl); (b) backscattered electron image (BSEI) of alkali feldspar with perthitic texture, VN-5; (c) diopside (Cpx) partially rimmed by allanite (Aln), VN-44, Xpl; (d) diopside crystal with an inclusion of biotite, and a thick rim with abundant inclusions of Fe-oxides (schiller-like structure), VN-5A, plane-polarized light (ppl); (e) diopside rimmed by hornblende, VN5A, ppl; (f) BSEI of hornblende (Hb) surrounding jimthompsonite (Jt), VN-5A.

Potassium feldspar appears mostly as anhedral to suhedral pokilitic crystals with inclusions of plagioclase and biotite. Its intergrowth with quartz in some samples gives rise to a granophyric/micrographic texture. Almost all K-feldspars display a perthitic to micro-perthitic texture, with plagioclase stringers (X_{Ab} = 0.78–0.99) constituting 15–26% by volume of the entire crystal (host composition: X_{Ab} = 0.06–0.29; Table 2; Figure 4b). In general, plagioclase stringers are slightly more sodic in granites compared to monzonites. In the granites and granodiorites, K-feldspar is more strongly affected by argillic alteration than coexisting plagioclase.

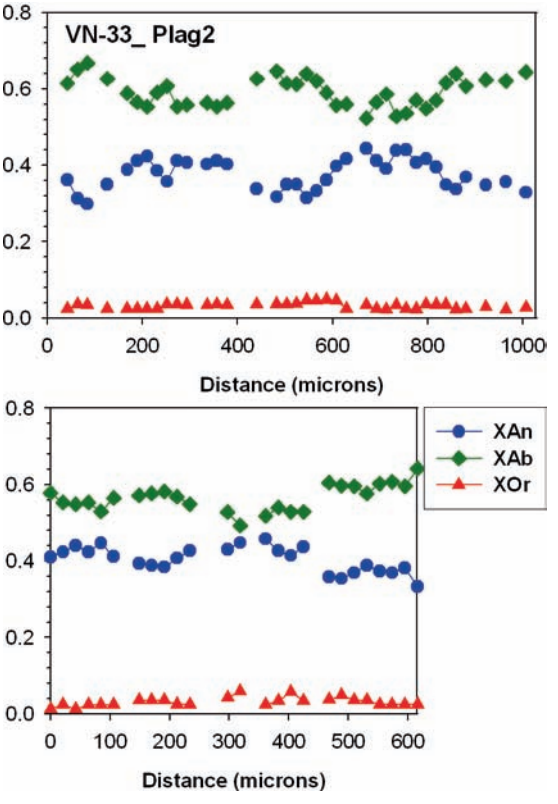

Figure 5. Zoning profile taken (a) along and (b) across a plagioclase crystal, VN-33.

Pyroxenes and amphiboles

Pyroxene is almost exclusively restricted to the monzonites/quartz monzonites, where it occurs as phenocrysts or cumulus crystals often mantled by hornblende or allanite (Figure 4c). In some samples, pyroxenes are characterized by clear cores surrounded by thick rims rich in inclusions/(exsolution lamellae?) of Fe-oxides giving rise to schiller-like/opacite-like structures commonly described for hornblende (e.g. Jakeš and White 1972; Figure 4d). Compositionally, these pyroxenes are mostly diopsides according to Morimoto *et al.* (1989) with a 'quad' component of 81–86%, a sodic component (jadeite+aegirine) of 6–13%, and X_{Mg} = 0.82–0.96. All crystals are homogeneous with the exception of the opacite-like rims, which are less magnesian (X_{Mg} = 0.73–0.82) and less calcic (Table 3).

Amphibole is ubiquitous, occurring as coarse-grained crystals that enclose apatite, Fe-oxides ± plagioclase ± titanite ± biotite ± K-feldspar. In a few samples (mainly monzonite), amphibole occurs as a cumulus phase (e.g. VN-19) or as phenocrysts (e.g. VN-41), often mantling diopside or jimthompsonite (Figure 4e and f). Compositionally, almost all amphiboles are magnesiohornblendes according to the classification of Leake *et al.* (1997), and are characterized by $Al^{iv} \sim 0.8 \pm 0.4$, and $X_{Mg} \sim 0.72 \pm 0.04$ (Table 4). A few hydrothermally altered granites (e.g. VN-9) are characterized by edenitic cores rimmed by actinolite (Al^{iv} = 0.3–0.4; X_{Mg} = 0.78–0.9; Table 4). In many samples, magnesiohornblende is partially to completely altered to actinolite, oxychlorite, calcite, haematite ± epidote.

Table 2. Representative feldspar compositions.

Sample no.	VN-2				VN-5		VN-33			VN-9				VN-2				VN-5		VN-33	
Analysis	1_5	1_9	1b_1	1b_8	40	34	35	45	109	2_18	2_20	2b_4	2b_6	12	18	16	17	36	81	50	52
		Core	Rim		Core	Rim	Rim	Core	Core					Kspar	Kspar	str	str	Kspar	str	Kspar	str
SiO_2	57.79	60.32	63.08	61.17	57.31	57.65	61.39	56.65	57.88	61.29	62.20	59.34	67.12	64.12	64.66	61.98	63.24	62.54	62.34	63.76	66.60
TiO_2	0.15	0.18	0.00	0.19	0.00	0.00	0.05	0.00	0.03	0.00	0.00	0.11	0.00	0.19	0.00	0.05	0.00	0.59	0.00	0.12	0.00
Al_2O_3	26.34	26.48	23.34	24.85	26.03	25.28	23.79	26.00	25.38	24.41	24.59	25.15	20.27	19.27	19.63	23.06	22.91	19.92	22.82	18.74	19.21
FeO	0.29	0.23	0.26	0.24	0.28	0.06	0.19	0.24	0.19	0.30	0.34	0.31	0.06	0.16	0.17	0.11	0.09	0.17	0.06	0.05	0.11
MgO	0.06	0.08	0.08	0.07	0.06	0.08	0.82	0.97	0.91	0.07	0.08	0.09	0.03	0.09	0.09	0.08	0.04	0.10	0.05	0.88	0.36
CaO	7.90	7.16	4.00	5.81	7.39	7.06	5.64	8.68	6.90	6.68	4.23	7.60	1.55	0.19	0.12	4.13	3.84	0.79	3.73	0.01	0.32
Na_2O	7.03	7.90	9.19	7.98	6.75	7.03	6.11	4.90	5.64	7.04	7.84	6.49	9.44	3.30	2.09	8.56	9.20	2.37	8.79	0.93	8.14
K_2O	0.38	0.41	0.23	0.49	0.37	0.32	0.38	0.15	0.56	0.15	0.21	0.15	0.30	12.07	14.06	0.33	0.73	12.62	0.35	15.09	1.16
Total	99.94	102.8	100.2	100.8	98.2	97.48	98.36	97.59	97.48	99.94	99.49	99.24	98.77	99.39	100.82	98.29	100.05	99.11	98.14	99.58	95.9
Si^{4+}	2.59	2.63	2.79	2.70	2.61	2.64	2.75	2.59	2.64	2.67	2.70	2.61	2.91	2.93	2.93	2.77	2.79	2.90	2.80	2.95	3.01
Ti^{4+}	0.01	0.01	0.00	0.01	0.00	0.00	0.00	0.00	0.00	0.00	0.00	0.00	0.00	0.01	0.00	0.00	0.00	0.02	0.00	0.00	0.00
Al^{3+}	1.39	1.36	1.22	1.29	1.40	1.36	1.26	1.40	1.36	1.33	1.34	1.39	1.11	1.04	1.05	1.21	1.19	1.09	1.21	1.02	1.02
Fe^{2+}	0.01	0.01	0.01	0.01	0.01	0.00	0.01	0.01	0.01	0.01	0.01	0.01	0.00	0.01	0.01	0.00	0.00	0.01	0.00	0.00	0.00
Mg^{2+}	0.00	0.01	0.01	0.00	0.00	0.01	0.05	0.07	0.06	0.00	0.01	0.01	0.00	0.01	0.01	0.01	0.00	0.01	0.00	0.06	0.02
Ca^{2+}	0.38	0.33	0.19	0.27	0.36	0.35	0.27	0.42	0.34	0.33	0.21	0.38	0.08	0.01	0.01	0.20	0.18	0.04	0.18	0.00	0.02
Na^{+}	0.61	0.67	0.79	0.68	0.60	0.62	0.53	0.43	0.50	0.63	0.70	0.59	0.85	0.29	0.18	0.74	0.79	0.21	0.77	0.08	0.71
K^{+}	0.02	0.02	0.01	0.03	0.02	0.02	0.02	0.01	0.03	0.01	0.01	0.01	0.02	0.70	0.81	0.02	0.04	0.75	0.02	0.89	0.07
Total	5.02	5.03	5.01	5.00	5.00	5.00	4.90	4.93	4.94	4.99	4.99	5.00	4.97	4.99	4.99	4.95	5.01	5.02	4.98	5.02	4.86
X_{An}	0.38	0.32	0.19	0.28	0.37	0.35	0.33	0.49	0.39	0.34	0.23	0.39	0.08	0.01	0.01	0.21	0.18	0.04	0.19	0.00	0.03
X_{Ab}	0.60	0.66	0.80	0.69	0.61	0.63	0.65	0.50	0.57	0.65	0.76	0.60	0.89	0.29	0.18	0.77	0.78	0.21	0.79	0.08	0.89
X_{Or}	0.02	0.02	0.01	0.03	0.02	0.02	0.02	0.01	0.03	0.01	0.01	0.01	0.02	0.70	0.81	0.02	0.04	0.75	0.02	0.92	0.09

Note: str, stringers or lamellae in perthite.

Table 3. Representative pyroxene compositions.

	VN-2							VN-5					
	21r	24r	25r	32c	33r	55	62	4	5	13	14	15	16
	Rim	Rim	Rim	Core	Rim			Core	Core	Core	Rim	Rim	Rim
SiO_2	53.31	51.72	50.45	52.68	49.02	48.27	49.75	49.58	50.08	49.79	50.87	50.94	51.63
TiO_2	0.56	0.70	0.67	0.29	1.16	1.73	0.63	0.86	0.65	0.63	0.18	0.56	0.46
Al_2O_3	6.40	2.98	2.95	2.01	6.42	6.74	3.49	3.23	2.76	2.79	1.55	2.61	2.28
Cr_2O_3	0.17	0.21	0.32	0.40	0.36	0.36	0.18	0.43	0.27	0.33	0.36	0.37	0.47
Fe_2O_3	0.00	4.46	2.80	4.20	1.94	3.54	5.78	5.19	5.86	4.88	4.08	5.74	3.86
FeO	4.45	4.18	5.37	2.90	9.91	8.71	2.86	4.93	1.22	3.26	4.12	2.74	3.92
MnO	0.51	0.56	0.12	0.85	0.83	0.57	0.44	0.57	1.20	0.84	0.92	0.58	1.16
MgO	18.01	14.73	14.00	14.21	15.06	14.97	14.69	12.90	14.73	14.12	13.09	13.98	14.85
CaO	14.00	20.73	20.03	22.68	11.94	11.93	20.20	20.87	20.93	19.93	21.54	21.44	20.87
Na_2O	1.65	1.06	1.04	1.10	1.46	1.73	1.01	1.04	1.07	1.14	1.08	1.23	0.83
Total	99.06	101.33	97.75	101.32	98.09	98.54	99.03	99.60	98.77	97.71	97.79	100.18	100.33
Si	1.93	1.89	1.91	1.92	1.85	1.81	1.86	1.86	1.87	1.89	1.94	1.89	1.91
Al^{iv}	0.07	0.11	0.09	0.08	0.15	0.19	0.14	0.14	0.12	0.11	0.06	0.11	0.09
T site	2.00	2.00	2.00	2.00	2.00	2.00	2.00	2.00	1.99	2.00	2.00	2.00	2.00
Al^{vi}	0.20	0.02	0.04	0.01	0.13	0.11	0.01	0.01	0.00	0.01	0.01	0.00	0.01
Ti	0.02	0.02	0.02	0.01	0.03	0.05	0.02	0.02	0.02	0.02	0.01	0.02	0.01
Cr	0.00	0.01	0.01	0.01	0.01	0.01	0.01	0.01	0.01	0.01	0.01	0.01	0.01
Fe^{3+}	0.00	0.12	0.08	0.12	0.05	0.10	0.16	0.15	0.16	0.14	0.12	0.16	0.11
Fe^{2+}	0.13	0.13	0.17	0.09	0.31	0.27	0.09	0.15	0.04	0.10	0.13	0.08	0.12
Mn^{2+}	0.02	0.02	0.00	0.03	0.03	0.02	0.01	0.02	0.04	0.03	0.03	0.02	0.04
Mg	0.97	0.80	0.79	0.77	0.85	0.84	0.82	0.72	0.82	0.80	0.74	0.77	0.82
Ca	0.54	0.81	0.81	0.89	0.48	0.48	0.81	0.84	0.84	0.81	0.88	0.85	0.83
Na	0.12	0.08	0.08	0.08	0.11	0.13	0.07	0.08	0.08	0.08	0.08	0.09	0.06
Jd + Ac	0.12	0.08	0.08	0.08	0.11	0.13	0.07	0.08	0.08	0.08	0.08	0.09	0.06
Q	0.79	0.83	0.85	0.85	0.78	0.74	0.80	0.81	0.81	0.82	0.85	0.81	0.86
X_{Wo}	0.34	0.48	0.47	0.52	0.30	0.32	0.50	0.51	0.51	0.49	0.51	0.52	0.48
X_{En}	0.58	0.45	0.44	0.43	0.52	0.52	0.45	0.41	0.47	0.46	0.42	0.44	0.46
X_{Fs}	0.08	0.07	0.09	0.05	0.18	0.16	0.05	0.08	0.02	0.06	0.07	0.04	0.06
Mg #	0.88	0.86	0.82	0.90	0.74	0.76	0.90	0.83	0.96	0.89	0.86	0.91	0.88

Table 4. Representative amphibole compositions.

Sample	VN-2							VN-5					
An. no.	36	37	52	53-r	56-m	57-r	61-c	26-r	61-r	93	108	59-c	75-c
Species	Mg-Hb	Mg-Hb	Mg-Hb	Mg-Hb	Mg-Hb	Mg-Hb	Mg-Hb	Mg-Hb	Mg-Hb	Edenite	Mg-Hb	Mg-Hb	Mg-Hb
SiO_2	46.99	47.30	49.42	48.84	47.72	46.02	48.40	48.54	47.36	48.02	48.29	51.98	51.41
TiO_2	1.30	1.41	1.04	0.96	1.23	1.34	0.96	0.72	0.83	0.77	0.27	0.44	0.35
Al_2O_3	7.59	6.71	5.73	5.52	6.27	6.84	5.54	5.43	5.56	5.62	5.48	3.02	3.62
Cr_2O_3	0.10	0.03	0.20	0.23	0.21	0.20	0.13	0.24	0.17	0.20	0.10	0.13	0.25
FeO	14.60	15.20	13.94	14.08	15.59	15.82	14.71	13.81	14.94	14.42	13.24	12.56	13.01
MnO	0.37	0.34	0.29	0.34	0.33	0.28	0.40	0.29	0.32	0.33	0.44	0.38	0.28
MgO	13.74	14.12	14.80	14.45	13.62	12.94	13.94	14.99	13.51	13.79	15.40	16.04	15.44
CaO	11.40	11.46	11.58	11.58	11.23	11.25	11.16	11.15	11.68	12.03	11.26	11.46	12.16
Na_2O	1.40	1.51	1.31	1.60	1.65	1.54	1.44	1.86	1.56	1.87	1.84	1.42	1.46
K_2O	0.57	0.62	0.41	0.30	0.56	0.70	0.41	0.30	0.35	0.43	0.37	0.01	0.05
Total	98.06	98.70	98.72	97.90	98.41	96.93	97.09	97.33	96.28	97.48	96.69	97.44	98.03
Si	6.79	6.81	7.05	7.07	6.91	6.80	7.06	7.03	7.03	7.07	7.02	7.45	7.40
Al^{iv}	1.21	1.14	0.95	0.93	1.07	1.19	0.94	0.93	0.97	0.93	0.94	0.51	0.60
Fe^{3+iv}	0.00	0.06	0.00	0.00	0.02	0.01	0.00	0.05	0.00	0.00	0.04	0.04	0.00
Al^{vi}	0.08	0.00	0.02	0.01	0.00	0.00	0.01	0.00	0.00	0.05	0.00	0.00	0.02
Cr	0.01	0.00	0.02	0.03	0.02	0.02	0.02	0.03	0.02	0.02	0.01	0.02	0.03
Fe^{3+}	0.81	0.82	0.70	0.60	0.75	0.75	0.74	0.75	0.53	0.28	0.82	0.53	0.30
Ti	0.14	0.15	0.11	0.10	0.13	0.15	0.11	0.08	0.09	0.09	0.03	0.05	0.04
Mg	2.96	3.03	3.15	3.12	2.94	2.85	3.03	3.23	2.99	3.03	3.34	3.43	3.31
Fe^{2+}	0.95	0.96	0.96	1.11	1.11	1.20	1.05	0.87	1.33	1.50	0.75	0.94	1.26
Mn	0.05	0.04	0.04	0.04	0.04	0.04	0.05	0.04	0.04	0.04	0.05	0.05	0.03
Ca	1.76	1.77	1.77	1.80	1.74	1.78	1.74	1.73	1.86	1.90	1.75	1.76	1.88
Na^B	0.24	0.23	0.23	0.21	0.26	0.22	0.26	0.27	0.14	0.10	0.25	0.24	0.12
Na^A	0.16	0.19	0.13	0.24	0.21	0.22	0.15	0.25	0.31	0.43	0.27	0.15	0.28
K^A	0.11	0.11	0.08	0.06	0.10	0.13	0.08	0.06	0.07	0.08	0.07	0.00	0.01
Fe^{3+} #	0.46	0.45	0.42	0.35	0.40	0.38	0.41	0.48	0.29	0.15	0.53	0.38	0.19
Fe*	0.37	0.38	0.35	0.35	0.39	0.41	0.37	0.34	0.38	0.37	0.33	0.31	0.32
Mg #	0.76	0.76	0.77	0.74	0.73	0.70	0.74	0.79	0.69	0.67	0.82	0.78	0.72

Table 4. (*Continued*).

Sample	VN-33								VN-9				
An. no.	83-c	58-r	12	1-c	4-r	8-r	12	14-r	19-r	21-r	22-r	24-c	25-r
Species	Edenite	Act	Act	Mg-Hb	Mg-Hb	Mg-Hb	Mg-Hb	Mg-Hb	Mg-Hb	Mg-Hb	Mg-Hb	Mg-Hb	Act
SiO_2	48.06	51.48	50.51	48.77	51.74	49.74	50.07	50.36	53.43	53.11	54.78	54.61	53.64
TiO_2	1.16	0.30	0.12	1.18	0.83	0.98	0.82	0.82	0.42	0.43	0.20	0.41	0.25
Al_2O_3	5.97	2.70	2.93	5.87	4.28	5.00	4.87	4.91	3.59	3.61	2.81	3.75	2.79
Cr_2O_3	0.15	0.11	0.23	0.06	0.19	0.04	0.08	0.17	0.14	0.13	0.01	0.19	0.24
FeO	12.19	13.54	16.70	12.53	10.77	12.80	11.62	11.43	8.53	8.84	7.27	8.35	9.33
MnO	0.22	0.33	0.18	0.67	0.41	0.65	0.44	0.51	0.12	0.17	0.17	0.17	0.11
MgO	14.94	14.60	12.69	15.02	16.55	15.88	16.33	16.02	17.90	17.60	18.86	18.42	17.41
CaO	13.57	12.54	11.99	11.70	12.19	11.40	11.95	11.91	11.88	12.04	11.71	10.97	11.63
Na_2O	1.75	1.28	1.19	1.85	1.44	1.69	1.96	1.53	1.60	1.53	1.45	1.60	1.18
K_2O	0.39	0.08	0.05	0.39	0.19	0.34	0.28	0.23	0.12	0.12	0.07	0.08	0.03
Total	98.40	96.96	96.59	98.04	98.59	98.52	98.42	97.89	97.73	97.58	97.33	98.55	96.61
Si	7.04	7.58	7.52	7.04	7.34	7.08	7.16	7.21	7.55	7.54	7.69	7.55	7.65
Al^{iv}	0.96	0.42	0.48	0.96	0.66	0.84	0.82	0.79	0.45	0.46	0.31	0.45	0.35
Fe^{3+iv}	0.00	0.00	0.00	0.00	0.00	0.08	0.02	0.00	0.00	0.00	0.00	0.00	0.00
Al^{vi}	0.07	0.04	0.04	0.04	0.06	0.00	0.00	0.04	0.15	0.15	0.16	0.16	0.12
Cr	0.02	0.01	0.03	0.01	0.02	0.01	0.01	0.02	0.02	0.02	0.00	0.02	0.03
Fe^{3+}	0.00	0.00	0.20	0.45	0.26	0.70	0.40	0.43	0.14	0.10	0.18	0.50	0.26
Ti	0.13	0.03	0.01	0.13	0.09	0.11	0.09	0.09	0.05	0.05	0.02	0.04	0.03
Mg	3.26	3.20	2.82	3.23	3.50	3.37	3.48	3.42	3.77	3.72	3.95	3.79	3.70
Fe^{2+}	1.49	1.67	1.88	1.06	1.02	0.74	0.97	0.94	0.87	0.95	0.68	0.47	0.85
Mn	0.03	0.04	0.02	0.08	0.05	0.08	0.05	0.06	0.01	0.02	0.02	0.02	0.01
Ca	2.00	1.98	1.91	1.81	1.85	1.74	1.83	1.83	1.80	1.83	1.76	1.62	1.78
Na^B	0.00	0.02	0.09	0.19	0.15	0.26	0.17	0.17	0.20	0.17	0.24	0.38	0.22
Na^A	0.50	0.34	0.26	0.33	0.25	0.21	0.37	0.25	0.24	0.25	0.16	0.05	0.10
K^A	0.07	0.02	0.01	0.07	0.03	0.06	0.05	0.04	0.02	0.02	0.01	0.01	0.01
Fe^{3+} #	0.00	0.00	0.10	0.30	0.20	0.51	0.30	0.31	0.14	0.10	0.21	0.52	0.24
Fe*	0.31	0.34	0.42	0.32	0.27	0.31	0.29	0.29	0.21	0.22	0.18	0.20	0.23
Mg #	0.69	0.66	0.60	0.75	0.77	0.82	0.78	0.78	0.813	0.797	0.854	0.890	0.813

Notes: c, core; r, rim; m, mantle around Cpx; Mg-Hb, magnesiohornblende; Ed, edenite; Act, actinolite; Fe^{3+} # = $Fe^{3+}/(Fe^{2+} + Fe^{3+})$; Fe* = $Fe_t/(Fe_t + Mg)$; Mg # = $Mg/(Fe^{2+} + Mg)$.
[A]The 10–12 coordinated site, [B]all 6–8 coordinated sites of the amphibole formula, $A_{0\text{-}1}\, B_7\, T_8\, O_{22}\, (OH, F, CL)_2$.

Biotite

Biotite occurs as medium- to coarse-grained crystals containing inclusions of apatite, magnetite, and ± zircon. It is typically more abundant in granites than coexisting hornblende, but in monzonites hornblende is usually more abundant (Table 1). In a few samples, biotite occurs as phenocrysts with hornblende and plagioclase (e.g. VN-44, VN-45). In altered samples, biotite is partially replaced by chlorite ± titanite/leucoxene ± Fe-oxide along its rims, but is generally less affected by alteration than the coexisting hornblende. Textures suggest that biotite crystallized later than hornblende and diopside in most samples, as attested to by coronas of biotite+Fe-oxide symplectites surrounding hornblende and diopside (Figure 6a and b). However, simultaneous crystallization of biotite, hornblende, and diopside in some monzonites (e.g. VN-20, VN-44) is supported by symplectic intergrowths and inclusion relations (Figures 4d, e and 6c). Compositionally, all biotites are Mg-rich (X_{Mg} = 0.58–0.65) with Al^{iv} = 2.1–2.4 on the basis of 22 oxygens per formula unit. The Ti^{vi} content of biotite is typically higher in the granites than in the monzonites and granodiorites (0.42–0.56 vs. 0.38–0.43, respectively; Table 5). Chlorine concentration ranges from 0.27 to 0.55 wt.%, with the highest values recorded in biotite from the monzonites.

Other minerals

The pyribole jimthompsonite (Table 5) occurs in some monzonite samples as polycrystalline masses of pale yellow, weakly pleochroic crystals with moderate relief, that appear to have replaced another mineral typically rimmed by hornblende (Figures 4f and 6d). Because diopside rimmed by hornblende occurs as pristine crystals in the same samples that contain jimthompsonite, we interpret the latter to have formed after orthopyroxene (cf. Jenkins 2009). Chlorine-rich apatite (chlorapatite?) and titanite are ubiquitous accessories, with the latter occurring as intergranular primary crystals (Figure 6e) or as a secondary phase forming at the expense of ilmenite (Figure 6f). Both generations of titanite are overall similar chemically (Table 6), although the primary titanite has higher Nb ± Zr, whereas the secondary variety is slightly more enriched in Fe. Allanite and zircon are quite common in most samples, usually occurring as sizeable intergranular phases (Figure 6g and i). In addition, zircon crystals are resorbed, and may be zoned as indicated by very subtle variations in average atomic number (Figure 6i and j). Magnetite and ilmenite are ubiquitous, usually concentrating along the rims of diopside, hornblende ± biotite. Titanhaematite ($X_{ilm} \leq 0.35$; Table 6) commonly replaces ilmenite along its rims. Rutile is rare, occurring in a few samples where it appears to have formed with titanhaematite at the expense of ilmenite (Figure 6h). Clinozoisite/epidote, calcite, and bastnäsite-Ce are rare secondary minerals that formed at the expense of plagioclase and allanite, respectively.

Figure 6. Selected textural relations: (a) diopside with 'opacite'-like rims showing schiller-like texture partially rimmed by a symplectite of biotite + Fe-oxides, VN-5A, ppl. (b) Diopside rimmed by hornblende partially overgrown by coarse-grained biotite, VN-2, ppl. (c) Symplectitic intergrowth between hornblende and biotite, VN-22, ppl. (d) Jimthompsonite (Jt) crystals in the core of hornblende, VN-19, ppl. Jimthompsonite is interpreted to have deuterically replaced orthopyroxene that was magmatically mantled by hornblende. (e) Intergranular crystals of 'primary' titanite and zircon surrounded by feldspars and quartz, VN-5, ppl. (f) Secondary titanite forming at the expense of ilmenite, VN-5, ppl. (g) Skeletal crystals of allanite partially enclosing orthoclase and apatite, VN-22, ppl. (h) BSEI of ilmenite (Ilm)-titanhaematite (Hem)-rutile (Rt) relations, VN-33. (i) BSEI of zircon with dissolved cores and subtle zoning (?), VN-2. (j) Zircon crystal with embayed outlines, partially dissolved core, and subtle zoning; VN-33.

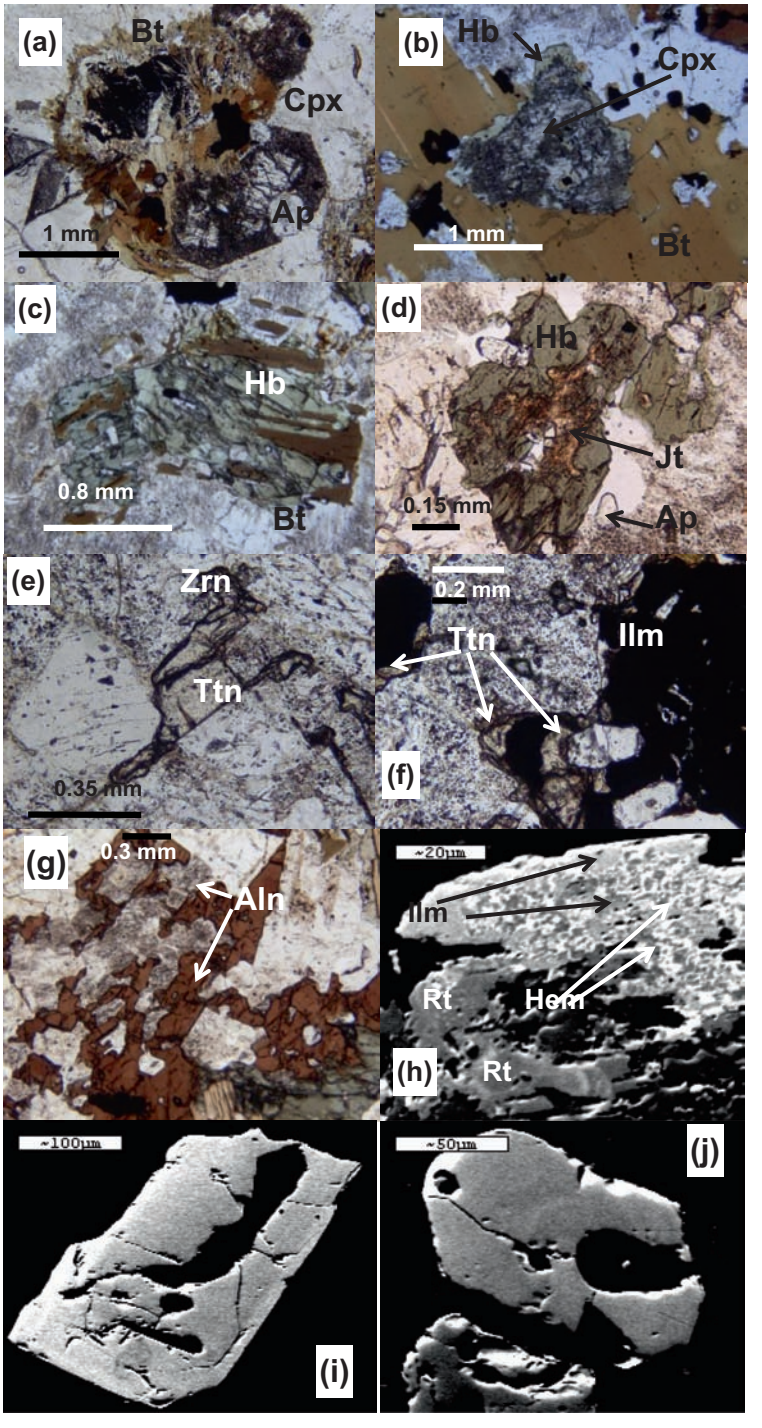

Table 5. Representative biotite and pyribole compositions.

	VN-2				VN-5		VN-33				VN-9			VN-5	106
	38	9 rim	41	42	28	29	9	10	59 c	60	1	2 rim	5	Jimthompsonite	
	Core	Rim	Core	Rim					Core	Rim	Core	Rim			
SiO_2	39.12	38.41	38.60	39.22	37.03	36.96	36.07	38.68	37.55	37.36	37.71	38.41	37.60		57.61
TiO_2	4.07	4.38	4.10	4.19	4.12	4.20	4.68	3.87	4.94	5.31	4.74	4.02	5.26		0.12
Al_2O_3	11.86	11.99	11.87	12.49	12.91	12.70	12.30	12.40	12.80	13.25	13.27	13.24	13.68		2.05
Cr_2O_3	0.09	0.00	0.00	0.00	0.03	0.03	0.00	0.06	0.00	0.00	0.10	0.08	0.00		0.06
FeO	14.78	15.19	14.55	14.74	15.40	15.49	16.56	16.14	16.31	16.58	14.29	16.09	15.85		14.92
MnO	0.09	0.09	0.14	0.19	0.06	0.24	0.00	0.00	0.09	0.00	0.08	0.00	0.02		0.25
MgO	15.21	15.37	15.70	15.59	15.42	15.33	13.64	15.05	13.83	13.16	15.16	15.26	14.36		21.06
CaO	0.08	0.03	0.06	0.05	0.04	0.10	0.11	0.00	0.00	0.03	0.12	0.00	0.00		0.00
Na_2O	0.29	0.31	0.18	0.60	0.62	0.55	0.48	0.19	0.35	0.38	0.25	0.15	0.20		1.46
K_2O	8.78	9.10	9.17	9.15	8.75	8.76	9.56	9.70	9.47	9.66	9.53	9.84	9.56		0.00
Cl	0.39	0.44	0.32	0.27	0.45	0.38	0.24	0.34	0.29	0.36	0.35	0.34	0.32		
H_2O	3.89	3.88	3.90	3.99	3.84	3.85	3.80	3.93	3.90	3.89	3.92	3.97	3.96		
Total	98.65	99.19	98.59	100.48	98.69	98.60	97.44	100.36	99.53	99.98	99.52	101.40	100.81		97.53
							22 (O)								17 (O)
Si	5.874	5.771	5.811	5.790	5.608	5.608	5.597	5.770	5.663	5.623	5.636	5.671	5.579		5.970
Al^{iv}	2.099	2.123	2.106	2.173	2.304	2.271	2.250	2.180	2.275	2.350	2.338	2.304	2.393		0.030
Al^{vi}	0.000	0.000	0.000	0.000	0.000	0.000	0.000	0.000	0.000	0.000	0.000	0.000	0.000		0.220
Ti	0.460	0.495	0.464	0.465	0.470	0.480	0.546	0.434	0.560	0.601	0.533	0.446	0.587		0.010
Cr	0.011	0.000	0.000	0.000	0.003	0.003	0.000	0.007	0.000	0.000	0.012	0.009	0.000		0.000
Fe	1.856	1.909	1.832	1.820	1.951	1.966	2.149	2.014	2.057	2.087	1.786	1.987	1.967		1.290
Mn	0.011	0.011	0.018	0.024	0.007	0.031	0.000	0.000	0.011	0.000	0.010	0.000	0.003		0.020
Mg	3.405	3.442	3.523	3.431	3.482	3.469	3.155	3.347	3.109	2.952	3.378	3.359	3.176		3.250
Ca	0.013	0.005	0.010	0.008	0.007	0.016	0.018	0.000	0.000	0.005	0.019	0.000	0.000		0.000
Na	0.084	0.090	0.053	0.172	0.183	0.163	0.144	0.055	0.102	0.111	0.072	0.043	0.058		0.200
K	1.682	1.744	1.761	1.723	1.691	1.695	1.892	1.846	1.822	1.854	1.817	1.853	1.809		0.000
OH*	3.901	3.888	3.918	3.932	3.883	3.901	3.937	3.914	3.926	3.908	3.911	3.915	3.920		
Cl	0.099	0.112	0.082	0.068	0.117	0.099	0.063	0.086	0.074	0.092	0.089	0.085	0.080		
Mg #	0.65	0.64	0.66	0.65	0.64	0.64	0.59	0.62	0.60	0.59	0.65	0.63	0.62		0.72

Table 6. Representative compositions of magnetite, ilmenite, and titanite.

	VN-2				VN-5								VN-33			VN-9
	30	47	49	54	31	102	103	67	71	72	30	66	54	63	65	15
	Hem	Ilm	Ilm	Mag	Mag	Mag	Mag	Ilm	Ilm	Ilm	Ttn_p	Ttn_s	Mag	Ilm	Hem	Mag
SiO_2	0.56	1.04	0.90	0.86	0.76	0.80	0.85	0.95	1.04	1.19	29.39	30.12	1.08	1.19	1.32	1.25
TiO_2	1.96	43.71	44.21	0.02	0.02	0.00	0.15	46.46	45.15	45.73	34.09	33.20	0.17	39.07	16.79	0.43
Al_2O_3	1.27	1.15	0.60	0.96	0.83	0.86	0.98	0.84	1.02	1.03	3.32	2.72	0.94	0.80	0.90	0.43
Cr_2O_3	0.00	0.00	0.00	0.43	0.45	0.15	0.17	0.00	0.00	0.00	0.00	0.00	0.00	0.00	0.00	0.01
Fe_2O_3	90.21	54.81	54.82	68.53	66.27	65.56	65.13	0.00	0.00	0.00	0.00	0.00	68.34	19.25	61.02	64.28
FeO	0.19	1.97	2.08	31.94	30.33	29.98	30.45	48.35	49.23	49.03	1.14	3.11	32.57	35.41	16.09	32.79
MnO	0.35	1.00	0.27	0.02	0.00	0.00	0.00	2.27	2.32	2.31	0.00	0.00	0.00	0.25	0.00	0.20
MgO	0.00	0.00	0.00	1.00	1.20	1.18	1.08	0.66	0.84	0.67	0.36	0.25	0.95	0.39	0.30	0.00
CaO	0.00	0.00	0.00	0.00	0.00	0.00	0.00	0.00	0.00	0.00	27.56	27.94	0.00	0.00	0.00	0.00
ZnO	0.00	0.00	0.00	0.07	0.00	0.00	0.00	0.00	0.00	0.00	0.00	0.00	0.04	0.00	0.00	0.00
Sum	94.54	103.68	102.88	103.83	99.86	98.54	98.80	99.53	99.60	99.96	95.86	97.34	104.09	96.36	96.42	99.39
Si	0.02	0.03	0.02	0.03	0.03	0.03	0.03	0.02	0.03	0.03	1.00	1.02	0.04	0.03	0.04	0.05
Ti	0.04	0.83	0.85	0.00	0.00	0.00	0.00	0.87	0.84	0.85	0.87	0.84	0.00	0.76	0.34	0.01
Al	0.04	0.03	0.02	0.04	0.04	0.04	0.04	0.02	0.03	0.03	0.13	0.11	0.04	0.02	0.03	0.02
Cr	0.00	0.00	0.00	0.01	0.01	0.00	0.01	0.00	0.00	0.00	0.00	0.00	0.00	0.00	0.00	0.00
Fe^{3+}	1.85	0.25	0.23	1.88	1.89	1.90	1.88	0.19	0.23	0.21	0.00	0.00	1.87	0.39	1.23	1.86
Fe^{2+}	0.05	0.84	0.87	0.98	0.96	0.96	0.98	0.82	0.79	0.81	0.03	0.09	0.99	0.77	0.36	1.05
Mn	0.01	0.02	0.01	0.00	0.00	0.00	0.00	0.05	0.05	0.05	0.00	0.00	0.00	0.01	0.00	0.01
Mg	0.00	0.00	0.00	0.05	0.07	0.07	0.06	0.02	0.03	0.02	0.02	0.01	0.05	0.02	0.01	0.00
Ca	0.00	0.00	0.00	0.00	0.00	0.00	0.00	0.00	0.00	0.00	1.00	1.01	0.00	0.00	0.00	0.00
X_{ilm}	0.045	0.835	0.860					0.845	0.815	0.830				0.195	0.350	
X_{hm}	0.925	0.125	0.115					0.095	0.115	0.105				0.765	0.612	
X_{sp}				0.049	0.068	0.068	0.058						0.038			
X_{ga}				0.000	0.000	0.000	0.000						0.000			
X_{usp}				0.000	0.000	0.000	0.000						0.000			
X_{mag}				0.979	0.979	0.979	0.979						0.979			0.984
X_{Hc}				0.000	0.000	0.000	0.000						0.000			0.011

Notes: Ttn_p, primary titanite; Ttn_s, secondary Ttn; ga, gahnite component.

Geochemistry

The analysed samples are characterized by average SiO_2 contents of 68 wt.% ± 1.2 for granites and 58.8 wt.% ± 2.2 for monzonites, average Al_2O_3 contents of 17.19 wt.% ± 0.97 for monzonites and 14.74 wt.% ± 0.43 for granites, and average MgO contents of 1.55% ± 0.19 in granites to 2.46 wt.% ± 0.98 in monzonites (Table 7). On the total alkali–silica diagram of Cox *et al.* (1979), the 'monzonites' and 'quartz monzonites' plot in the syenodiorite, syenite, and monzonite fields, the 'granites' and 'granodiorites' plot in the granite and quartz diorite fields, whereas the dikes are syenitic, consistent with Sanderson's (1972) petrographic analysis. Almost all samples are quartz- and hypersthene-normative; only VN-20 and VN-44 show normative olivine.

Based on Frost *et al.*'s (2001) three-tier major-element classification scheme, all samples are magnesian, calcalkaline, and either metaluminous or mildly peraluminous (Figure 7). All mildly peraluminous samples (characterized by alumina saturation index and A/CNK $[Al_2O_3/(CaO + Na_2O + K_2O)]$ >1 but <1.2) were collected from the margins of the pluton (Figures 2 and 7c). On the SiO_2–K_2O plot of Peccerillo and Taylor (1976), the monzonites are shoshonitic whereas the granites and granodiorites are high-K calcalkalic (Figure 8).

Harker-type variation diagrams for MgO, FeO_t, TiO_2, CaO, V, Y, La, and Ce all show near-continuous trends (save for a gap between 62 and 65 wt.% SiO_2) with negative slopes, with some clustering of data points for the SiO_2-rich granites and granodiorites (Figures 9 and 10). On the other hand, plots of Al_2O_3, Na_2O, K_2O, Sr and Ba versus SiO_2 show two distinct trends (exclusive of the cumulate samples VN-44 and VN-26): a positive correlation displayed by the monzonites and a negative correlation/distinct cluster displayed by the granodiorites and granites (Figures 9 and 10). On REE plots, all samples show light rare earth element (LREE)-enriched patterns with slight negative Eu anomalies. This REE enrichment is 10–100 times relative to chondrite values, and is highest for the monzonites (Figure 11).

P–T–fO_2 conditions of magma crystallization and emplacement

Thermobarometric results

Pressure and temperature conditions of crystallization/mineral equilibration in rocks are typically calculated from the application of several experimentally constrained thermobarometers. Anderson (1996) summarized the applicability of several geothermobarometers to granitic batholiths and their potential pitfalls. Whereas temperatures of crystallization or mineral equilibration in the Melrose Stock may be constrained by applying several well-calibrated geothermometers (e.g. two-feldspar geothermometer, Stormer 1975; Fuhrman and Lindsley 1988; magnetite-ilmenite thermometer, Buddington and Lindsley 1964; Spencer and Lindsley 1981; zirconium saturation thermometer, Watson and Harrison 1983; quartz-titanite-magnetite thermometer, Wones 1989; and hornblende-plagioclase thermometer, e.g. Holland and Blundy 1994), pressures can only be calculated using the 'Al-in-hornblende' geobarometer (e.g. Hammarstrom and Zen 1986; Hollister *et al.* 1987; Johnson and Rutherford 1989; Anderson and Smith 1995).

Application of the two-feldspar geothermometer to the quartz monzonite samples VN-2 and VN-5 at P = 2.2 kbar (see below) using program 'Solvcalc' (Wen and Nekvasil 1994), after re-integration of the albite stringers of perthite into their host K-rich alkali feldspar yields temperatures of 780–820°C or 750–765°C, using the solution models of Elkins and Grove (1990) or Fuhrman and Lindsley (1988), respectively. The granitic sample VN-33

Table 7. Major- and trace-element analyses of 30 samples from the Melrose Stock.

	Granites														Granodiorites	
Sample	VN-7	VN-8	VN-9	VN-11	VN-16	VN-23	VN-24	VN-25	VN-30	VN-31	VN-33	VN-45	VN-47	VN-37	VN-12	VN-29
SiO_2	69.12	65.00	67.53	68.70	68.56	69.20	66.7	68.30	68.55	68.97	69.61	67.83	67.54	67.57	68.07	65.70
TiO_2	0.43	0.61	0.61	0.43	0.55	0.55	0.60	0.63	0.58	0.57	0.52	0.59	0.53	0.50	0.51	0.69
Al_2O_3	14.33	15.05	15.40	14.35	14.49	14.48	15.16	14.34	14.99	14.89	15.29	14.67	13.93	14.93	14.61	13.91
Fe_2O_3	2.53	3.99	3.18	2.96	3.05	3.66	3.71	3.35	3.39	3.41	3.10	3.48	3.43	2.98	3.41	2.18
MnO	0.03	0.04	0.02	0.04	0.04	0.06	0.04	0.04	0.04	0.04	0.03	0.06	0.04	0.04	0.05	0.05
MgO	1.20	1.64	1.56	1.43	1.69	1.72	1.86	1.57	1.57	1.65	1.24	1.63	1.60	1.34	1.54	2.15
CaO	2.08	3.10	3.30	2.32	2.73	3.29	2.87	2.79	2.98	2.33	2.88	3.20	2.59	2.58	3.31	4.26
Na_2O	3.62	3.57	3.30	3.28	3.09	3.65	2.98	3.41	3.05	3.01	3.39	3.00	3.35	3.78	3.84	3.94
K_2O	4.96	4.35	4.51	4.92	3.16	3.77	3.61	4.05	3.48	3.41	4.28	4.42	4.46	5.40	3.87	4.57
P_2O_5	0.15	0.21	0.24	0.24	0.48	0.32	0.44	0.19	0.47	0.47	0.39	0.24	0.25	0.28	0.33	0.24
LOI	0.85	0.57	0.55	0.81	0.68	0.54	0.71	0.73	1.05	1.02	1.09	0.74	0.51	0.78	0.49	0.79
Total	99.3	98.1	100.2	99.5	98.5	101.2	98.7	99.4	100.2	99.8	101.8	99.8	98.2	100.2	100.0	98.5
Yb	1.26		1.88	1.96	1.9	1.53	2.02	1.60	1.9	1.57		1.9	1.56	1.54	1.75	1.85
Zr	339		252	239	200	214	245	231	239	216		350	193	270	207	251
Y	13.9		19.5	16.7	20.5	17.3	22.4	16.4	20.5	16.6		19.6	17.4	17.8	19.5	22.0
Sr	598.5		718.3	666.2	640.4	594.7	658.9	550.7	607.9	605.9		682.1	574.8	679.8	683.8	618.0
Ba	1273		1372	1027	1091	1064	1224	952.7	994	1088		1368	1193	1767	1022	1226
Ta			23.2		17.1	41.2	16.6		19.7	16.5				21.2	34.8	19.1
Hf			6.5		5.3	6	7.2		6.9	5.9				6.9	5.8	6.7
Th			40.3		29.4	23.9	33.7		31.9	27				38.6	33.2	36.5
Nb	43.2		63.5	35.04	52.3	52.3	52.5	73.92	60.7	45.4		62.88	58.56	54	64.5	57.3
Rb	128.1		162.7	186.8	140.5	143.6	155.3	168.8	160.6	145.3		197.3	180.6	172.5	157.7	134.7
V			68		68	71	91		74	73				66	66	77
LI	22.42	17.66	19.28	21.38	18.83	18.51	17.75	19.42	18.71	19.33	20.56	19.06	19.67	21.3	18.62	18.07
SI	9.748	12.13	12.44	11.36	15.38	13.41	15.31	12.68	13.66	14.37	10.31	13	12.46	9.916	12.15	16.76
NFI	87.96	82.1	79.72	85.16	81.15	81.6	80.38	81.66	79.83	84.31	82.14	89.09	79.22	84.81	83.18	89.91

Table 7. (*Continued*).

	Granodiorites		Monzonites											
Sample	VN-34	VN-40	VN-2	VN-5	VN-19	VN-20	VN-21	VN-22	VN-26	VN-32	VN-41	VN-42	VN-44	VN-15
SiO_2	66.92	66.99	59.35	61.73	59.31	58.71	60.72	60.81	55.65	59.73	58.51	58.05	54.27	64.88
TiO_2	0.54	0.53	0.78	0.57	0.88	0.77	0.73	0.69	1.00	0.77	0.81	0.86	1.07	0.52
Al_2O_3	14.22	15.37	16.05	19.27	17.11	17.76	18.35	17.61	16.36	16.66	16.66	16.56	16.70	16.43
Fe_2O_3	3.64	3.01	5.28	2.43	4.84	5.13	3.99	4.27	7.05	3.40	5.95	4.67	7.14	3.09
MnO	0.05	0.50	0.07	0.03	0.07	0.10	0.08	0.08	0.12	0.06	0.36	0.05	0.12	0.04
MgO	1.46	1.70	2.58	1.29	1.46	2.17	1.72	1.67	4.27	2.55	2.42	2.98	3.99	1.05
CaO	2.68	3.17	4.86	3.36	3.03	3.97	3.04	3.51	6.16	4.31	4.90	5.39	7.18	2.00
Na_2O	3.21	3.41	3.93	4.99	4.11	4.73	4.29	4.92	3.34	4.67	4.14	4.35	4.06	3.91
K_2O	4.56	4.59	4.34	5.16	5.82	5.82	5.19	5.93	3.47	4.67	4.72	5.01	4.47	5.25
P_2O_5	0.32	0.24	0.32	0.24	0.23	0.42	0.24	0.35	0.47	0.24	0.62	0.64	0.76	0.46
LOI	0.81	0.62	0.72	0.93	0.81	0.72	0.47	0.53	0.71	2.27	0.49	1.02	0.75	0.83
Total	98.4	100.1	98.3	100.0	97.7	100.3	98.8	100.4	98.6	99.3	99.6	99.6	100.5	98.5
Yb	1.67	1.69	2.21	1.43	2.75	2.58	2.06		2.27	2.71	2.799	2.26	2.71	2.13
Zr	247	189	384	473	663	252	502		228	289	619	394	407	544
Y	17.0	18.3	24.5	15.6	23.4	22.7	25.1		28.4	22.9	25.9	26.8	34.3	22.4
Sr	567.2	699.1	1008.2	1207.8	998.0	971.9	872.9		1237.7	986.1	963.4	919.8	1203.2	489.1
Ba	969	1252	1474	1781	2199	1831	1719		1840	1648	1300	1683	1896	762
Ta			30.3	8.8			29.5		9.4			11.4	13.3	16.9
Hf			8.8	11.4			11.9		6.5			8.1	9.3	12.8
Th			66.4	65.1			44		63.3			51.6	64.7	105.1
Nb	36.96	35.52	105.6	74.2	38.48	41.28	84.7		89.9	40.32	60.48	97.3	86.3	137.1
Rb	177.5	179.4	179.4	160.9	255.6	264.7	183.1		168.6	218.9	295.1	181.7	171.3	275.4
V			127	75			86		170			132	174	61
LI	19.43	19.32	11.91	18.89	16.72	14.61	17.06	17.16	5.228	14.63	11.53	11.76	4.952	21.03
SI	11.33	13.4	16	9.278	8.996	12.16	11.32	9.947	23.54	16.7	14.05	17.54	20.29	7.892
NFI	83.2	81.07	81.54	82.96	86.23	88.11	83.21	90.07	71.54	86.25	82.95	85.94	81.12	90.26

Notes: Major-element data in wt.%, trace-element data in ppm.
LI, Larsen index; SI, solidification index; NFI, normative felsic index; LOI, loss on ignition.

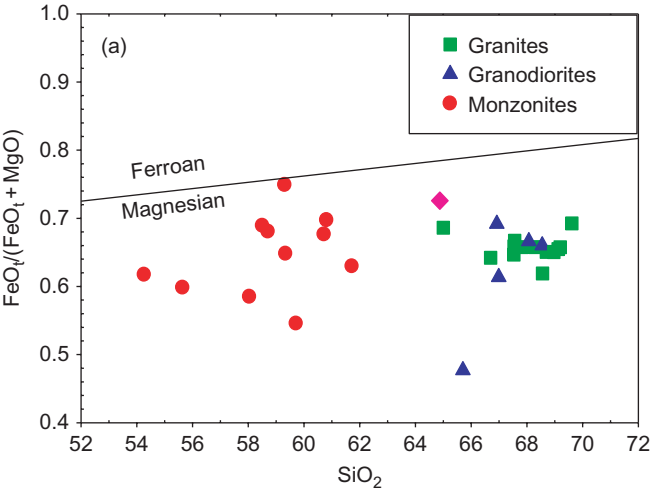

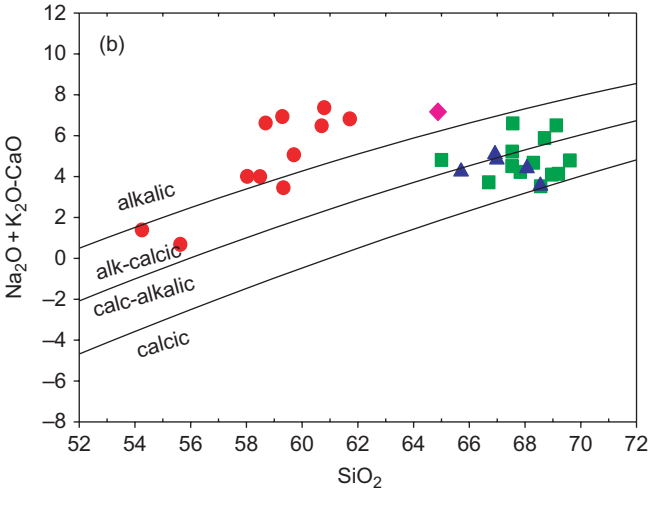

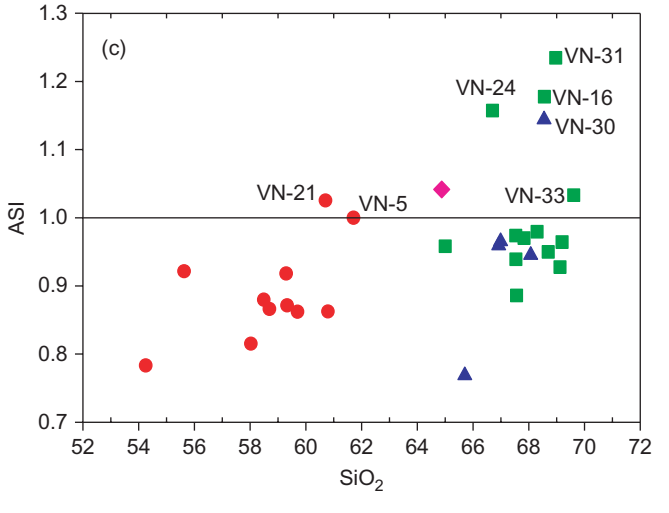

yielded higher temperatures (820–830°C) using these two models (Table 8). Application of the zircon saturation thermometer of Watson and Harrison (1983) to the bulk rock compositions of all analysed samples yields temperatures of 806 ± 48°C, 789 ± 21°C, and 809 ± 18°C for the monzonites, granodiorites, and granites, respectively, and 890°C for the syenitic dike VN-15. These temperatures are typically slightly higher than those obtained through the application of the two-feldspar geothermometer for the same sample (802 vs. 760°C for VN-2; and 853 vs. 820°C for VN-5; Table 8).

The magnetite-ilmenite thermometer of Spencer and Lindsley (1981) can only be applied to samples that have not been affected by post-crystallization oxidation, hydrothermal alteration, or weathering. Among the five samples selected for microprobe analysis, VN-33, VN-34, and VN-9 show clear evidence of subsolidus oxidative breakdown of ilmenite to titanhaematite and rutile (Figure 6h), giving rise to textures similar to those of stages R3–R5 (e.g. Haggerty 1991; Lindsley 1991). Applying the Spencer and Lindsley (1981) thermobarometer to a single magnetite crystal with $X_{Usp} = 0.08$ and ilmenite with average X_{ilm} of 0.88 in VN-5 ($X_{Hm} = 0.09$–0.11; Table 6) yields a T of 680°C and $\log fO_2 = -15$. Using the ilmenite-haematite solvus at the Ni–NiO buffer of Lindsley (1991), the haematite content of ilmenite in VN-5 yields a temperature of 850°C. Application of the activity-corrected equilibrium between quartz, titanite, magnetite, clinopyroxene, and ilmenite (Wones 1989; Anderson 1996), using the ideal mixing on sites model for activity calculations, yields fO_2 values in the range $10^{-13.5}$ to $10^{-8.8}$ between P and T conditions of 700°C, 1 kbar, and 850°C, 2.2 kbar, respectively, indicating conditions about 3.75 log units above the Ni–NiO buffer.

The Al-in-hornblende barometer is suitable for calculating pressures for calcalkalic rocks with the assemblage hornblende ($Fe^{3+}/(Fe^{3+} + Fe^{2+}) > 0.25$, $X_{mg} > 0.35$), plagioclase ($X_{An} = 0.25$–0.35), biotite, K-feldspar, and primary titanite and magnetite or ilmenite, that crystallized at $T < 800$°C, and fO_2 conditions at or above the Ni–NiO buffer (Anderson and Smith 1995). Although all five samples selected for microprobe analysis fulfil these criteria, samples VN-9 and VN-33 show evidence of hydrothermal alteration that has resulted in the formation of significant amounts of actinolite along the rims of hornblende. Application of this barometer in conjunction with the plagioclase-hornblende thermometers of Holland and Blundy (1994) to samples VN-2, VN-5, and VN-34 yields an optimum P of 1.8–2.3 kbar at T of 680–760°C (Anderson and Smith 1995). Table 8 lists the results obtained from the application of the various thermobarometers discussed above.

Interpretation of P–T–fO$_2$ data

The apparent discrepancy in the temperatures obtained for the same sample using different thermobarometers is to some extent expected, given the duration over which the magma cooled and crystallized, and the variety of factors that may have interfered with the minerals equilibrating at a unique temperature. Nevertheless, P–T conditions of emplacement of the stock can be estimated with some confidence, as long as they are consistent with field and petrologic constraints. The occurrence of two separate feldspars in these rocks indicates

Figure 7. (a) SiO_2 versus $FeO_t/(FeO_t + MgO)$; line marks the boundary between ferroan and magnesian granites according to Frost *et al.* (2001). (b) SiO_2 versus modified alkali lime index of Frost *et al.* (2001); curves mark boundaries between alkalic, alkali-calcic, calc-alkalic, and calcic fields. (c) SiO_2 versus alumina saturation index (ASI) of Frost *et al.* (2001). Note that all labelled samples plotting as 'low peraluminous' (ASI > 1) are from the margins of the pluton, and are interpreted to have been affected by assimilation of pelitic country rocks.

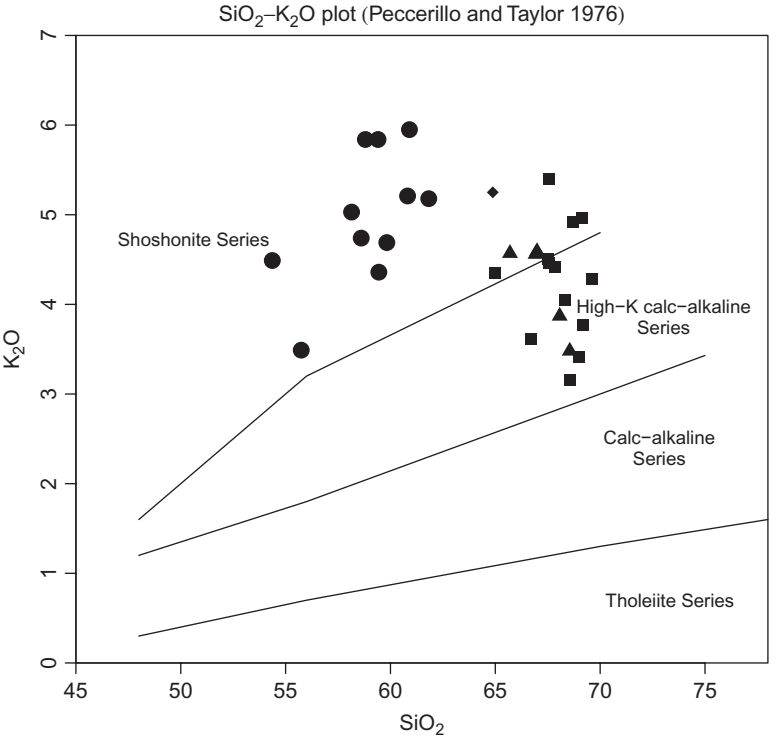

Figure 8. SiO_2 versus K_2O plot of Peccerillo and Taylor (1976), showing Melrose granitoids as high K calc-alkaline to shoshonitic. Symbols are as in Figure 3.

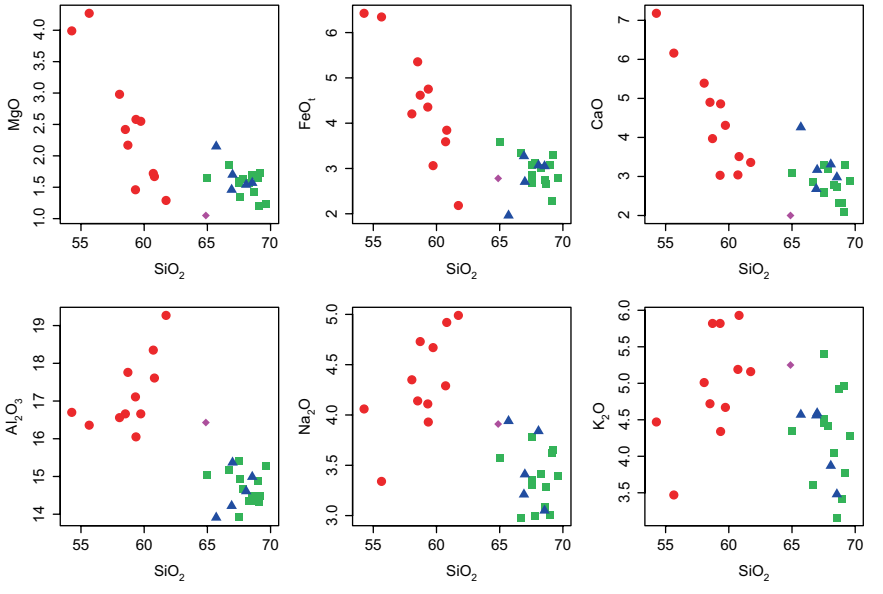

Figure 9. Major-element Harker-type variation diagrams. Symbols are as in Figure 3. All concentrations are in wt.%.

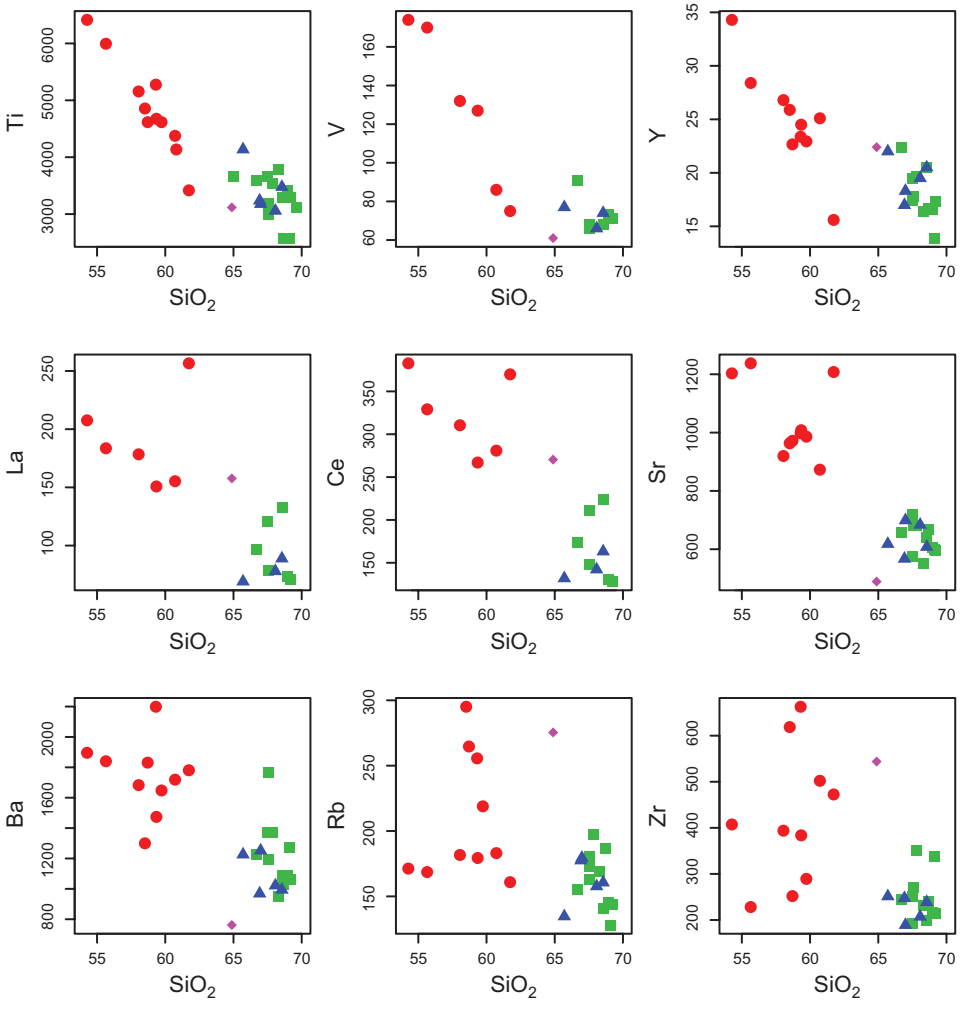

Figure 10. Trace-element variation diagrams. Symbols are as in Figure 3. All concentrations are in ppm.

that the stock is at least mesozonal, implying depths of emplacement in excess of *ca*. 5 km. On the other hand, textural relations between iron oxides and rutile (Figure 6h) that are similar to stages R3–R4–R5 of the oxidative breakdown of ilmenite to rutile + haematite indicate minimum temperatures of 600°C (Haggerty 1991; Lindsley 1991). The occurrence of jimthompsonite in some samples is also consistent with these results, as similar pyriboles form at *T* of 600°C or less, typically at the expense of enstatite, diopside, or anthophyllite (Schumacher and Czank 1987; Ams *et al.* 2009; Jenkins 2009).

Zirconium saturation thermometry is designed to constrain liquidus temperatures, and assumes that there was no inherited zircon in the magma (Watson and Harrison 1983). Although the zircon crystals observed in the Melrose Stock samples are typically intergranular, some are characterized by resorbed edges, dissolved cores, and possible growth zoning (Figure 6i and j). These disequilibrium textures, which are more common in the monzonites, lead us to conclude that Zr saturation temperatures in these rocks can only be considered maximum estimates for the crystallization of the Melrose Stock, as some zircons may indeed have been inherited.

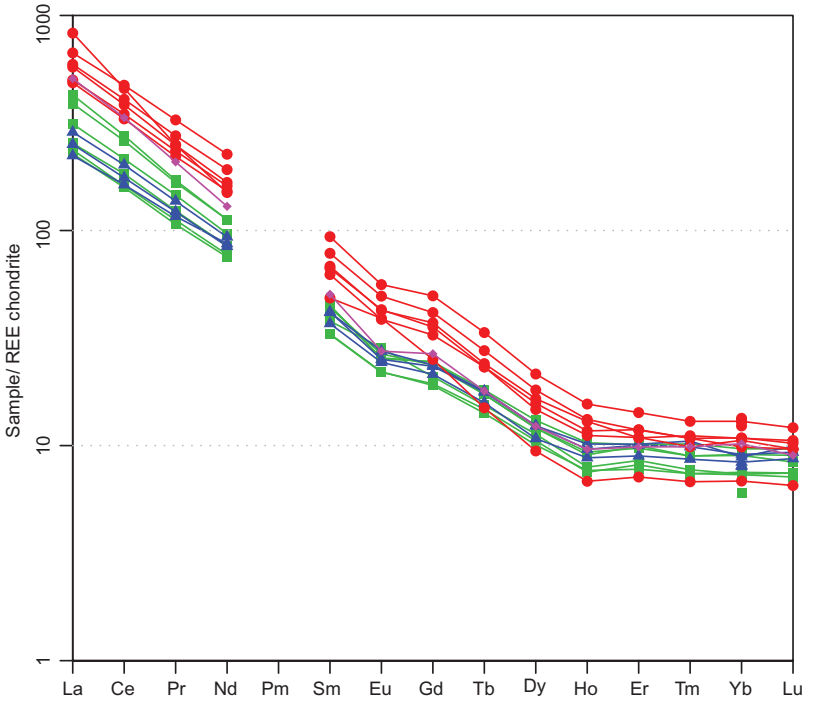

Figure 11. Chondrite normalized rare earth element diagram for select Melrose Stock samples. Symbols are as in Figure 3. Normalization values are from Sun and McDonough (1989).

Temperatures calculated using the ulvospinel content of magnetite are fraught with significant uncertainty given that most magnetites are characterized by very low X_{Usp} (typically 0; Table 6). On the other hand, the use of the ilmenite-haematite join of Lindsley (1991) alone for temperature estimation requires *a priori* knowledge of fO_2. Although it is reasonable to assume that fO_2 conditions were constrained by the Ni–NiO buffer (given that the rocks belong to the magnetite series of Ishihara (1977)), higher values of fO_2 are equally likely,

Table 8. Results of thermobarometry.

Sample	Zr sat. T[a]	2 feldspar	Mgt-Ilm[b]	Ilm-Hm[c]	Hb-Plg	P[d] (kbar)
VN-5	853	759–765[e] 780–830[g]	650	850	680–780[f] 660–810[h]	2.2 0.3–1
VN-2	802	750–780[e] 785–790[g]	<600	650	790–810[f] 700–720[h]	1.2–2.2 2.2–2.4
VN-34	805	645[e] 670[g]		620–650	580–670[f] 580–690[h]	1.7–1.9
VN-33		750–760[e] 730–745[g]		NA	635–765[f] 675–720[h]	0.6–1.1 0.6–1.1
VN-9	805	630[e] 645[g]	NA	NA	635[f] 720[h]	1–2.2

Notes: [a]Watson and Harrison (1983); [b]T based on ulvospinel content of magnetite, Spencer and Lindsley (1981); [c]T based on X_{ilm} at NiNiO buffer, Lindsley (1991); [d]P estimated using the Al-in-hornblende barometer of Anderson and Smith (1995); [e]Fuhrman and Lindsley (1988); [f]edenite + quartz = tremolite + albite, Holland and Blundy (1994); [g]Elkins and Grove (1990); [h]edenite + albite = richterite + anorthite, Holland and Blundy (1994).

and will result in lower *T* estimates, leading us to conclude that the *T* of 850°C obtained for VN-5 (Table 8) is only a maximum temperature.

Although the temperatures obtained from the application of two-feldspar thermometry are broadly consistent with those calculated using hornblende-plagioclase/Al-in-hornblende thermobarometry, we consider this to be fortuitous, since the former constrains temperatures of crystallization (having relied on anorthite-rich cores and integrated alkali feldspar compositions), whereas the latter constrains the conditions of emplacement (having utilized average plagioclase and hornblende rim compositions). Because temperatures obtained using the Elkins and Grove (1990) solution models for the two-feldspar thermometer are closer to Zr saturation temperatures, this formulation is favoured, and leads us to conclude that crystallization of the monzonite-quartz monzonite magma began at *T* of ~800°C at $P > 2.3$ kbar. Oxygen fugacity conditions prevailing during crystallization (and emplacement?) of this stock are estimated at ~3.75 log units above the Ni–NiO buffer as constrained by the application of the titanite-quartz-magnetite-clinopyroxene-ilmenite equilibrium of Wones (1989). These relatively high fO_2 values are consistent with the high REE content of 'primary' titanite (e.g. Piccoli *et al.* 2000), evidenced by their energy dispersive spectra and their low major oxide totals (Table 6).

Pressure–temperature conditions of emplacement of the same magma are estimated at 680–780°C and 1.5–2.3 kbar based on hornblende-plagioclase and Al-in-hornblende thermobarometry (Holland and Blundy 1994; Anderson and Smith 1995; Table 8). Lower *P–T* conditions obtained for samples VN-34, VN-33, and VN-9 are considered highly suspect, given that these samples were affected by hydrothermal alteration. On the other hand, if the syenite dike represents a Zr saturated melt extracted from a crystal mush deeper than the stock, it may have crystallized at *T* close to 890°C. These results are considered preliminary, as more mineral analysis is needed to constrain the conditions of crystallization and emplacement of the more differentiated rock types, and identify any inter-pluton variations in $P–T–fO_2$ conditions.

Petrogenesis of the Melrose Stock

Major- and trace-element modelling

The nearly continuous trends displayed by most major- and trace-element variation diagrams (Figures 9 and 10) lead to the suggestion that all rock types of the Melrose Stock are cogenetic. This interpretation is strongly supported by the REE and spider diagrams (Figures 11 and 13), which indicate that all rocks evolved from the same magma in the same tectonic environment. The overall curvilinear trends on the MgO, FeO_t, CaO, and TiO_2 versus SiO_2 variation diagrams are consistent with the fractional crystallization of mafic minerals, whereas the sharp kinks in the Al_2O_3, Na_2O, and K_2O variation diagrams (Figure 9) are best explained by the late fractionation of alkali feldspars. These fractionation trends can therefore be tested by modelling, provided that the compositions of the initial magma, proposed fractionating phases, and final differentiation product are reasonably known or estimated. This requires the identification of the least- and most-differentiated samples within the stock.

Many methods have been proposed for identifying how differentiated a rock is (cf. Cox *et al.* 1979; Winter 2010 for review). In this study, we used a combination of Larsen's index (Larsen 1938), the solidification index (Kuno 1959), the differentiation index (Thornton and Tuttle 1960), and the normative felsic index [100(ab + or)/(ab + or + an)]. Values of these indices show that sample VN-7 is the most differentiated (having one of the lowest solidification index values, highest Larsen index, and a high normative felsic

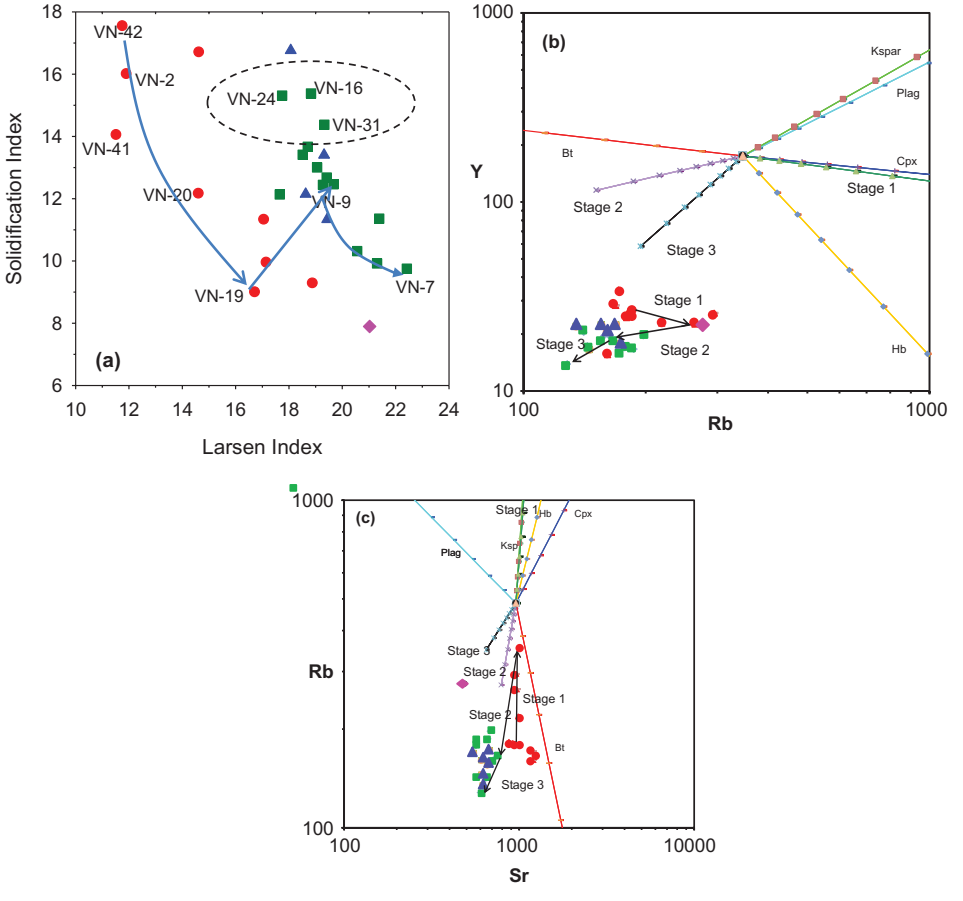

Figure 12. (a) Plot of solidification index ($100 \times MgO/(MgO + Fe_2O_3 + Na_2O + K_2O)$) versus Larsen index ($1/3SiO_2 + K_2O - MgO - CaO - FeO_t$). Symbols are as in Figure 3. Arrows designate the differentiation trends discussed in text. Dashed oval encloses some of the samples from the margin of the stock most affected by assimilation. (b) Logarithmic plot of Y versus Rb. Symbols are as in Figure 3. Vectors designate the three stages of differentiation discussed in the text. Results of trace-element modelling are also indicated schematically, where Stage 1 marks the fractionation of 24% Cpx, 3% Pl, and 3% Hb; Stage 2 that of 25% Bt, 19% Hb, 6% Pl, and 6% Kfs; and Stage 3 of 20% Hb, 16% Bt, 2% Pl, and 2% Kfs. Every tick mark on mineral vectors represents 10% crystallization. (c) Logarithmic plot of Sr versus Rb. Symbols are as in Figure 3. Vectors designate the three stages of differentiation discussed in text. Results of trace-element modelling are also indicated schematically, where Stage 1 marks the fractionation of 33% Cpx, 15% Pl, and 2.5% Hb; Stage 2 that of 40% Bt, 25% Hb, and 35% Pl; and Stage 3 of 12% Hb, 17% Bt, and 20% Pl. Every tick mark on mineral vectors represents 10% crystallization.

index), whereas VN-26 and VN-45 are the least differentiated (Table 7; Figure 12a). Because the latter two samples are characterized by cumulus textures, neither one is considered a suitable representative of the parent magma. Instead, samples VN-41 and VN-42 seem more appropriate choices, despite having a porphyritic texture with phenocrysts of hornblende and plagioclase. VN-42 was therefore selected to represent the parent magma because of its location on most variation diagrams and its higher solidification index compared to VN-41 (Table 7; Figure 12a).

Major-element modelling was carried out with Petrograph (Petrelli *et al.* 2005), which uses the mass balance algorithm of Stormer and Nicholls (1978). Cumulus minerals and phenocrysts in monzonites were selected as the fractionating phases, and their compositions were constrained from SEM analysis (Tables 2–6). All major- and minor-element oxides were included in the algorithm except P_2O_5, given the low sensitivity of the ICP detecting the 213.618 nm line for *P* and the subsequent analytical uncertainties. Results of modelling were considered acceptable if the sum of the squared residuals (SSR) reflecting the differences between the compositions of the initial magma on one hand and the fractionating phases + the final product on the other is <1.

All attempts at modelling the differentiation of a parent magma represented by VN-42 to a final product represented by VN-7 through one-step fractionation of pyroxene, hornblende, plagioclase ± biotite ± magnetite ± ilmenite ± titanite failed, either by yielding high SSR values (~9–10) or by requiring the addition of hornblende ± titanite. On the other hand, kinks on a plot of the solidification index versus Larsen index, variation diagrams, and trace-element bivariate plots (Figures 9, 10, and 12) are indeed consistent with the parent magma having undergone more than one stage of fractionation. In fact, plots of K_2O and Na_2O versus SiO_2, and Rb versus Sr and Y, all show three discrete 'segments', each of which possibly represents a distinct stage of fractionation (Figure 12), namely: (1) from VN-42 to a cluster of data points including VN-19, VN-21, and VN-20, (2) from the 'VN-19 data cluster' to another cluster including VN-9, VN-25, VN-47, etc.; and (3) from the 'VN-9 cluster' to VN-7. Testing this three-stage evolution (VN-42 → VN-19 → VN-9 → VN-7) through major-element modelling using actual analyses of feldspars, diopside, hornblende, biotite, and K-feldspar from samples VN-2 and VN-5 suggests that Stages 1–3 were accomplished through the fractionation of clinopyroxene + plagioclase, hornblende + K-feldspar + plagioclase, and plagioclase + hornblende + K-feldspar+biotite, respectively (Table 9). Although these results are broadly consistent with petrographic observations, the value of SSR for Stage 2 is too high to be acceptable (4.59), and the total amount of fractionating biotite calculated by this model (<2%) is unrealistically small, given that this mineral is a common phenocryst in some monzonites.

Attempts to model the three-segment trends on the logarithmic bivariate plots of Rb versus Y and Sr versus Rb were carried out using FC-Modeler (Keskin 2002) and partition coefficients (K_d) for intermediate magmas compiled by Keskin (1994). The results are only broadly consistent with those obtained by major-element modelling, suggesting an early stage of fractionation of clinopyroxene > plagioclase, followed by a stage of fractionation of biotite > hornblende > plagioclase, and a third stage involving the fractionation of plagioclase, hornblende, and biotite, possibly in sub-equal amounts (Table 9). Although the results of trace-element modelling are more realistic than those of major-element modelling,

Table 9. Results of major- and trace-element modelling.

	Stage 1	Stage 2	Stage 3
	VN-42 → VN-19	VN-19 → VN-9	VN-9 → VN-7
Major	12% Cpx, 11% Pl	15% Pl, 21% Hb, 40% Kfs	9% Pl, 6% Hb, 0.25% Bt, 2% Kfs
SSR	0.57	4.59	0.5
Rb-Y	24% Cpx, 3% Pl, 3% Hb	6% Pl, 19% Hb, 6% Kfs, 25% Bt	2% Pl, 20% Hb, 16% Bt, 2% Kfs
Sr-Rb	33% Cpx, 15% Pl, 2.5% Hb	35% Pl, 25% Hb, 40% Bt	20% Pl, 12% Hb, 17% Bt

Note: SSR, sum of the squared residuals.

there are still major problems as well as significant discrepancies between the Rb–Y and Sr–Rb models. Whereas some discrepancies may be due to the use of inappropriate K_d values, particularly when the fractionating plagioclase and the magma are known to change in composition through the three stages, the amount of fractionating phases suggested for Stage 2 is unrealistically high (56–100%, Table 9). This suggests that a differentiation mechanism other than fractional crystallization should be explored to account for the evolution of the magma during Stage 2.

The oscillatory zoning displayed by most coarse-grained plagioclase crystals in nearly all samples and the resorbed nature of some of these zones are similar to Type II zoning of Pearce and Kolisnik (1990), which indicates disequilibrium between some of these zones and the magma. Opacite-like rims on diopside are also indicative of disequilibrium (e.g. Jakeš and White 1972). Disequilibrium responsible for these two textures is typically attributed to changes in PH_2O due to cyclic eruptions (e.g. Loomis 1982), local changes accompanying crystallization (e.g. Piccoli *et al.* 2000), or injection of hot magma into a cooling and crystallizing magma chamber (e.g. Tepley *et al.* 1999; Winter 2010). Because there is no evidence to support any of these scenarios in the Melrose Stock, we suggest that oscillatory zoning in feldspars and opacite-like rims on diopside developed through the interaction of these phenocrysts with more differentiated liquids within the same magma chamber. We argue that such interaction was brought about by the stratified nature of the magma chamber, followed by the onset of convection, leading to the entrainment of plagioclase and diopside phenocrysts through the compositionally distinct layers with which they had not equilibrated (e.g. Blundy and Shimizu 1991). This would account for the curvilinear segments representing Stage 2 on logarithmic trace-element bivariate plots (Figure 12b and c), which are typically interpreted as indicative of 'mixing' (e.g. Keskin 2002).

Tectonic setting of magma generation and emplacement

Major- and trace-element compositions of igneous rocks are commonly used to identify the origin and tectonic setting of their magmas with the help of spider and discriminant diagrams (e.g. Pearce *et al.* 1984; Maniar and Piccoli 1989; Sun and McDonough 1989). Spider diagrams of normal mid-oceanic ridge basalt (N-MORB)-normalized trace-element concentrations for the Melrose Stock samples show relatively high values for incompatible large-ion lithophile elements (LILEs), a clear spike for the high-field-strength elements (HFSEs) Th and U, and significant troughs for Nb, P, and Ti (Figure 13a). Plots of the same concentrations normalized to ocean ridge granites (ORG) on the spider diagram of Pearce *et al.* (1984) show LILE enrichment, a double spike for Rb and Th, and smaller humps for Ce and Sm (Figure 13b), a pattern very similar to those shown by some volcanic arcs (e.g. Chile; Pearce *et al.* 1984). On the other hand, all samples from the Melrose Stock plot as 'within-plate granites' on the trace-element discriminant diagrams of Pearce *et al.* (1984), despite the fact that their Y and Yb contents are characteristic of arc-related magmas (Figure 14).

Application of the empirical method of Maniar and Piccoli (1989) to the Melrose Stock samples suggests that most rocks are 'orogenic' with either island arc (IAG) or volcanic arc (VAG) affinities. A few samples are characterized by A/CNK values >1.05, and may possibly be continental collisional granites (CCGs) according to this scheme. Moreover, most samples overlap with the field of 'Cordilleran granites' on diagrams of Frost *et al.* (2001), whereas the monzonites plot as 'late orogenic' granitoids on the R_1–R_2 classification scheme of Batchelor and Bowden (1985) (Figure 15).

The results listed above lead us to the conclusion that the Melrose Stock granitoids formed in a volcanic arc setting late in the orogenic cycle, rather than as anorogenic,

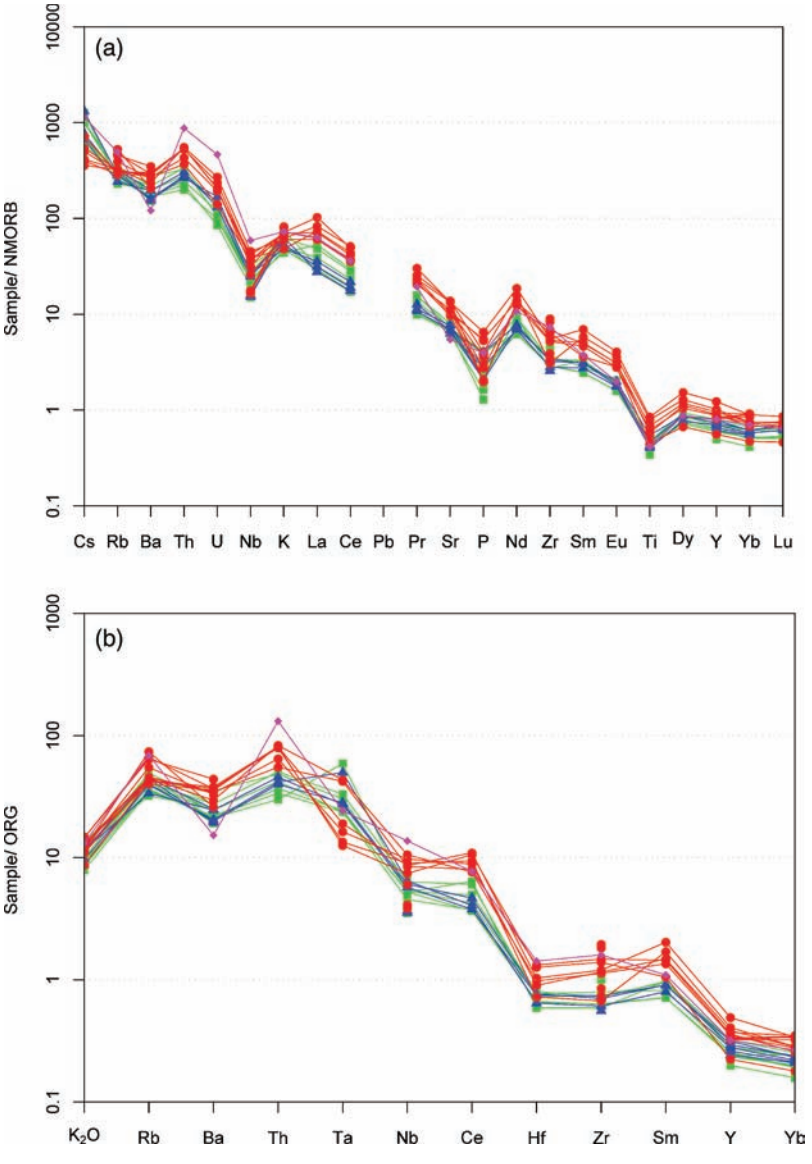

Figure 13. (a) N-MORB normalized spider diagram of Sun and McDonough (1989). Normalization factors from Boynton (1984). (b) Ocean ridge granite (ORG) normalized spider diagram of Pearce *et al.* (1984). Symbols as in Figure 3.

within plate granitoids. The spikes and humps displayed by the LILEs on spider diagrams suggest that the magma was likely generated in the presence of H_2O-rich fluids, whereas the 'troughs' for Ti, Nb, and P suggest that these elements were sequestered by solids during magma generation. Both observations are consistent with the generation of the parent magma by partial melting of metasomatized peridotite in the mantle wedge atop a subducting slab where minerals such as rutile and pyroxene were stable (e.g. Drummond and Defant 1990; Tatsumi and Eggins 1995). The apparent discrepancy with the trace-element

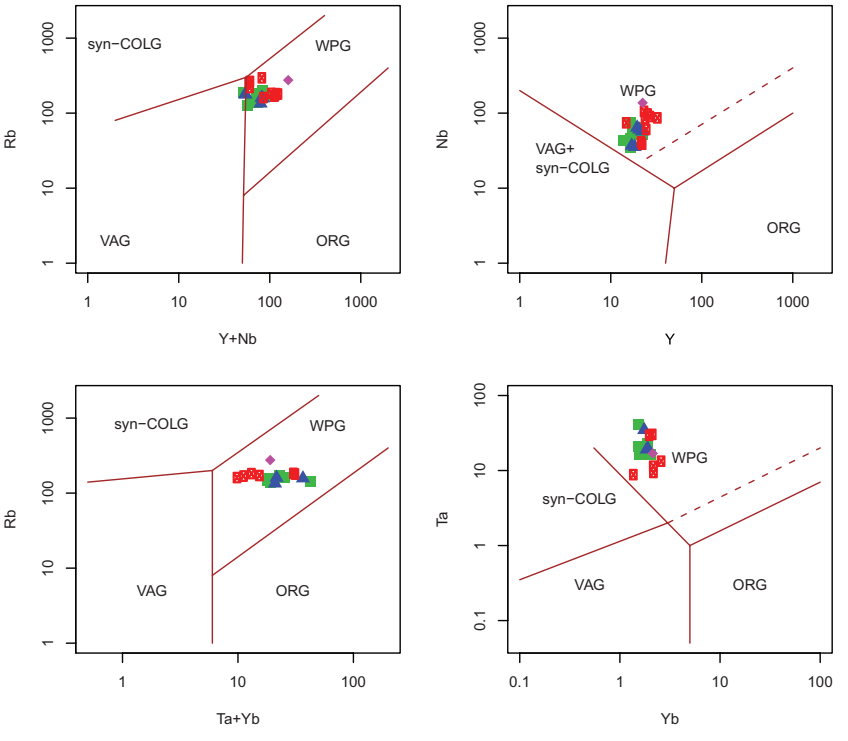

Figure 14. Trace-element discriminant plots of Pearce *el al.* (1984). Symbols as in Figure 3.

discrimination plots of Pearce *et al.* (1984) that suggest a 'within-plate origin' for the Melrose Stock can be accounted for by the presence of significant amounts (up to 2 vol.%) of accessory titanite and allanite which concentrate Nb, Y, and Ta. Moreover, Pearce (1996) showed that post-collisional granites overlap in part with 'within-plate granites' on Y+Nb versus Rb diagrams. This in turn suggests that major-element discriminant diagrams similar to those of Maniar and Piccoli (1989) and Batchelor and Bowden (1985) are better suited for identifying the tectonic setting of granitoids, as suggested by Frost *et al.* (2001).

Although a few samples (VN-16, -24, -30, and -31) are characterized by A/CNK values >1.05, and may possibly be CCGs according to the classification scheme of Maniar and Piccoli (1989), we have ruled out this possibility as these samples are from the margin of the stock and were most likely affected by assimilation of country rocks (Figure 2). On the other hand, the R_1–R_2 diagram of Batchelor and Bowden (1985) also shows the evolution of the Melrose monzonitic magma through an orogenic cycle where the least differentiated (VN-26 and VN-41) and most differentiated (VN-19) samples define a trend towards the origin, consistent with their differentiation from a mantle-derived basic magma (Batchelor and Bowden 1985) before evolving to the more acidic compositions (e.g. VN-9 and VN-7; Figure 15).

Magmatic evolution and petrotectonic interpretations

Despite the preliminary nature of some aspects of this study, field, petrographic, mineral chemical, thermobarometric, and major- and trace-element compositional data all indicate that the Melrose Stock consists of subsolvus, magnetite series, mesozonal granitoids. Their

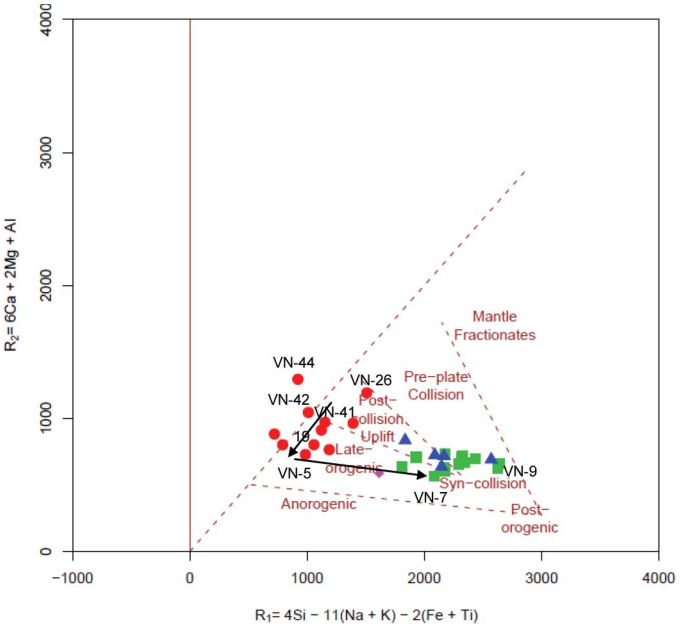

Figure 15. Cationic plot of R_1 [4Si – 11(Na + K) – 2(Fe + Ti)] versus R_2 (6Ca + 2Mg + Al) showing all monzonites falling in the fields of post-collisional/late orogenic granitoids. Differentiation trends are indicated by arrows. Symbols as in Figure 3.

petrographic characteristics, along with their metaluminous, calcalkaline, and magnesian nature, are consistent with those of I-type granites as defined by Chappell and White (1974). Zirconium saturation temperatures for these rocks (~804 ± 36°C) fall between those values for the 'hot' and 'cold granites' of Miller *et al.* (2003), but place them well within the 'low *T*' category of Chappell *et al.* (2004). Nevertheless, Melrose Stock samples have several chemical and petrographic characteristics that are very similar to those of the 'high *T*, I-type granites' of these authors (e.g. bimodal SiO_2 contents, curvilinear trends on bivariate plots, even distribution of mafic minerals, interstitial nature of quartz, and common occurrence of hornblende with corroded cores of clinopyroxene). More data are therefore needed for the positive identification of the Melrose Stock rocks as either 'low-temperature' or 'high-temperature' I-type granitoids.

Tectonically, parental magmas for the Melrose rocks were derived from the mantle in a subduction zone setting. The monzonitic magma was probably emplaced late in the orogenic cycle after significant 'hybridization' with continental crust, as indicated by the rocks falling in the 'high K calcalkalic' to 'shoshonitic' fields of Peccerillo and Taylor (1976) (Figure 8). The Melrose Stock rocks are therefore considered 'transitional' or 'hybrid mixed origin late orogenic (H_{Lo})' according to the classifications of Winter (2010) and Barbarin (1990), respectively.

We therefore suggest that the parent magma of the Melrose Stock was likely an olivine tholeiite generated by partial melting of mantle peridotite metasomatized by H_2O-rich fluids released from an east-dipping subducted slab. As the magma ascended through the mantle it differentiated through the fractional crystallization of olivine, pyroxene ± plagioclase, probably during a period of subduction rollback late in the cycle of the Elko orogeny (Thorman *et al.* 1992). The resulting magma likely ponded at the crust–mantle boundary

before intruding the continental crust thinned by ongoing extension in the back-arc area of an outboard island arc to the west (Thorman *et al.* 1992). As the magma intruded the continental crust, it underwent more differentiation through fractional crystallization and assimilation of crustal material. The onset of crystallization ~165 Ma (Zamudio 1993) took place at $T \sim 800°C$.

By the time of its final emplacement at P of 2.3–1.8 kbar and T of 750–700°C, this hybrid magma was monzonitic in composition. The first stage (Stage 1) of post-emplacement magmatic evolution may have been marked by fractional crystallization (partly through crystal settling?) of pyroxene + plagioclase, coupled with limited assimilation of pelitic country rocks along the roof and margins of the intrusion, which resulted in local increases in PH_2O and fO_2 within the chamber. This in turn caused the stratification of the magma into layers each with distinct thermal and compositional properties. As the magma continued to cool and crystallize, convection ensued, possibly in response to thermogravitational instability between the different layers. As a result, different layers in the magma chamber began to mix, causing plagioclase feldspars that had crystallized earlier to undergo a series of repeated phases of partial resorption and recrystallization to produce the oscillatory zoning observed in most samples (Figure 4a). This 'mixing' process, which characterizes Stage 2 of differentiation (Figure 12), led to the partial, localized breakdown of pyroxene to magnetite (Figure 4d). This stage was also accompanied by the fractionation of plagioclase, hornblende, and biotite, which would account for the complex textures between the latter two minerals (e.g. Figures 6a and c). As the magma continued to cool, more biotite and hornblende fractionated, probably under increased fO_2 conditions to produce the more differentiated granites and granodiorites (Stage 3, Figure 12). The highly differentiated syenite dikes represented by VN-15 would then correspond to a felsic melt extracted from a crystal mush at depths significantly greater than those represented by the samples studied (e.g. Bachmann and Bergantz 2008).

Following the complete crystallization of the magma, and as the temperature dropped below 650°C, the rocks underwent significant deuteric alteration. This is manifested by the localized oxidative breakdown of ilmenite first to secondary titanite ± magnetite (Figure 6f), then to rutile + haematite (Figure 6h), the subsolidus crystallization of jimthompsonite at the expense of orthopyroxene (Figures 4f and 6d), and the development of perthitic and myrmekitic textures. Late-stage hydrothermal alteration resulted in the localized saussuritization and chloritization of feldspar and biotite, respectively, and the formation of actinolite along the rims of hornblende.

Conclusions

- The Melrose Stock rocks are subsolvus, magnetite series, I-type granitoids.
- All rocks are magnesian, metaluminous, high K-calcalkalic to shoshonitic in composition, with a subduction zone signature. These petrological and chemical characteristics are similar to those of transitional or hybrid late-orogenic granitoids.
- Parental magma was a basalt generated by partial melting of metasomatized peridotite in the mantle wedge of an arc. This basaltic magma rose to shallower levels during fore-arc extension, possibly in response to subduction rollback and development of a new subduction zone to the west of an approaching island arc. This magma differentiated during its ascent through fractional crystallization and contamination with continental crust.
- The resulting monzonitic magma intruded the crust late in the Elko orogeny during a period of extension (Thorman *et al.* 1992), rather than one of modest shortening as

suggested by Miller and Hoisch (1992). The magma was emplaced at a relatively shallow depth of 5–7 km at $T \sim 750–700°C$.

- The monzonitic magma continued to evolve by fractional crystallization of pyroxene + plagioclase to produce some cumulates and a deeper crystal mush. Assimilation, convection-induced mixing, and fractionation of plagioclase, hornblende, and biotite produced the granodiorites and granites, which crystallized under more oxidizing and water saturated conditions, as suggested by Sanderson (1972).

Acknowledgements

All discriminant and classification diagrams were prepared using GCD-kit (Janousek *et al*. 2006). Financial support was provided by the Geology Department at Marshall University and through start-up funds from the university to El-Shazly. Part of this research was carried out as a capstone project for Jeff Napier and Adam Sholes in partial fulfilment of their BS degrees at Marshall University. Chloe Wonnel assisted with sample preparation/digestion. Reviews by J. Webster and T. Vogel helped improve this manuscript. Any remaining errors are the sole responsibility of the authors.

References

Afifi, A.M., and Essene, E.J., 1988, MINFILE: A microcomputer program for storage and manipulation of chemical data on minerals: American Mineralogist, v. 73, p. 446–447.

Ams, B., Jenkins, D.M., Boerio-Goates, J., Morcos, R.M., Navrotsky, A., and Bozhilov, K.N., 2009, Thermochemistry of a synthetic Na–Mg-rich triple chain silicate: Determination of thermodynamic variables: American Mineralogist, v. 94, p. 1242–1254.

Anderson, J.L., 1996, Status of thermobarometry in granitic batholiths, in Brown, M., Candela, P.A., Peck, D.L., Stephens, W.E., Walker, R.J., and Zen, E-an, eds., The Third Hutton Symposium on the Origin of Granites and Related Rocks: Geological Society of America Special Paper, v. 315, p. 125–138.

Anderson, J.L., and Smith, D.R., 1995, The effects of temperature and fO_2 on the Al-in-hornblende barometer: American Mineralogist, v. 80, p. 549–559.

Armstrong, R.L., 1963, Geochronology and geology of the Eastern Great Basin [Ph.D. thesis]: New Haven, CT, Yale University.

Armstrong, R.L., 1988, Mesozoic and early Cenozoic magmatic evolution of the Canadian Cordillera, in Clark, S.P., Burchfiel, B.C., and Suppe, J., eds., Processes in continental lithospheric deformation: Geological Society of America Special Paper, p. 218.

Bachmann, O., and Bergantz, G.W., 2008, Rhyolites and their source mushes across tectonic settings: Journal of Petrology, v. 49, p. 2277–2285.

Barbarin, B., 1990, Granitoids: Main petrogenetic classifications in relation to origin and tectonic setting: Geological Journal, v. 25, p. 227–238.

Barton, M.D., 1990, Cretaceous magmatism, metamorphism, and metallogeny in the east-central Great Basin, in Anderson, J.L., ed., The nature and origin of Cordilleran magmatism: Geological Society of America, Memoir, v. 174, p. 283–302.

Batchelor, R.A., and Bowden, P., 1985, Petrogenetic interpretation of granitoid rock series multicationic parameters: Chemical Geology, v. 48, p. 43–55.

Blundy, J.D., and Shimizu, N., 1991, Trace element evidence for plagioclase recycling in calc-alkaline magmas: Earth and Planetary Science Letters, v. 102, p. 178–197.

Boynton, W.V., 1984, in Henderson, P., ed., Rare earth element geochemistry: Amsterdam, Elsevier, p. 63–114.

Briggs, P.H., 2002, Determination of 27 elements in aqueous samples by inductively coupled plasma-atomic emission spectroscopy, *in* Taggart, J.E., ed., Analytical methods for chemical analysis of geologic and other materials: USGS Open File Report 02-0223.

Buddington, A.F., and Lindsley, D.L., 1964, Iron–titanium oxide minerals and synthetic equivalents: Journal of Petrology, v. 5, p. 310–357.

Chappell, B.W., and White, A., 1974, Two contrasting granite types: Pacific Geology, v. 8, p. 173–174.

Chappell, B.W., White, A.J., Williams, I.S., and Wyborn, D., 2004, Low- and high-temperature granites: Transactions of the Royal Society of Edinburgh, Earth Science, v. 95, p. 125–140.

Condie, K.C., 1989, Plate tectonics and crustal evolution (third edition): Oxford, New York, Pergamon Press, 476 p.
Cox, K.G., Bell, J.D., and Pankhurst, R.J., 1979, The interpretation of igneous rocks: London, George Allen and Unwin, 450 p.
De La Roche, H., Leterrier, J., Grandclaude, P., and Marchal, M., 1980, A classification of volcanic and plutonic rocks using R_1R_2 diagram and major-element analysis – its relationships with current nomenclature: Chemical Geology, v. 29, p. 183–210.
Drummond, M.S., and Defant, M.J., 1990, A model for trondhjemite–tonalite–dacite genesis and crustal growth via slab melting: Archean to modern comparisons: Journal of Geophysical Research, v. 95, p. 21503–21521.
Elison, M.E., 1991, Intracontinental contraction in western North America: Continuity and episodicity: Geological Society of America Bulletin, v. 103, p. 1226–1238.
Elkins, L.T., and Grove, T.L., 1990, Ternary feldspar experiments and thermodynamic models: American Mineralogist, v. 75, p. 544–559.
Frost, B.R., Barnes, C., Collins, W.J., Arculus, R.J., Ellis, D.J., and Frost, C.D., 2001, A geochemical classification for granitic rocks: Journal of Petrology, v. 42, p. 2033–2048.
Fuhrman, M.L., and Lindsley, D.L., 1988, Ternary-feldspar modeling and thermometry: American Mineralogist, v. 73, p. 201–215.
Haggerty, S.E., 1991, Oxide textures: A mini-atlas, in Lindsley, D.H., ed., Oxide minerals: Petrologic and magnetic significance: Reviews in Mineralogy, v. 25, p. 129–219.
Hammarstrom, J.M., and Zen, E-an, 1986, Aluminum in hornblende: An empirical geobarometer: American Mineralogist, v. 71, p. 1297–1313.
Holland, T.J.B., and Blundy, J., 1994, Non-ideal interactions in calcic amphiboles and their bearing on amphibole–plagioclase thermometry: Contributions to Mineralogy and Petrology, v. 116, p. 433–447.
Hollister, L.S., Grissom, G.C., Peters, E.K., Stowell, H.H., and Sisson, V.B., 1987, Confirmation of the empirical correlation of aluminum in hornblende with pressure of solidification of calc-alkaline plutons: American Mineralogist, v. 72, p. 231–239.
Ingamells, C.O., 1966, Absorptiometric methods in rapid silicate analysis: Analytical Chemistry, v. 38, p. 1228–1234.
Ishihara, S., 1977, The magnetite-series and ilmenite-series granitic rocks: Mining Geology, v. 27, p. 293–305.
Jakeš, P., and White, A.J.R., 1972, Hornblendes from calcalkaline volcanic rocks of island arcs and continental margins: American Mineralogist, v. 57, p. 887–902.
Janousek, V., Farrow, C.M., and Erban, V., 2006, Interpretation of whole-rock geochemical data in igneous geochemistry: Introducing Geochemical Data Toolkit (GCDkit): Journal of Petrology, v. 47, p. 1255–1259.
Jenkins, D., 2009, Predicting the formation conditions of the triple chain silicate sodic clino-jimthompsonite: Geological Society of America, Abstracts with Programs, v. 41, no. 7, p. 637.
Johnson, M.C., and Rutherford, M.J., 1989, Experimental calibration of the aluminum-in-hornblende geobarometer with application to Long Valley Caldera (California) volcanic rocks: Geology, v. 17, p. 837–841.
Keskin, M., 1994, Genesis of collission-related volcanism on the Erzurum-kars plateau, northeastern Turkey [PhD thesis]: Durham, University of Durham, 358 p. Keskin, M., 2002, FC-modeller: a Microsoft Excel® speadsheet program for modelling Rayleigh fractionation vectors in closed magmatic systems: Computers and Geosciences, v. 28, p. 919–928.
Kistler, R.W., 1990, Two different lithosphere types in the Sierra Nevada, California, in Anderson, J.L., ed., The nature and origin of Cordilleran magmatism: Geological Society of America, Memoir, v. 174, p. 271–281.
Kretz, R., 1983, Symbols for rock-forming minerals: American Mineralogist, v. 68, p. 277–279.
Kuno, H., 1959, Origin of Cenozoic petrographic provinces of Japan and surrounding areas: Bulletin of Volcanology, v. 20, p. 37–76.
Larsen, E.S., Jr., 1938, Some new variation diagrams for groups of igneous rocks: Journal of Geology, v. 46, p. 505–520.
Leake, B.E., *et al*., 1997, Nomenclature of amphiboles: report of the Subcommittee on Amphiboles of the International Mineralogical Association, Commission on New Minerals and Mineral Names: The Canadian Mineralogist v. 35, p. 219–246.
Le Maitre, R.W., Streckeisen, A., Zanettin, B., Le Bas, M.J., Bonin, B., Bateman, P., Bellieni, G., Dudek, A., Efremova, S., Keller, J., Lameyre, J., Sabine, P.A., Schmid, R., Sørensen, H., and

Wooley, A.R., 2002, Igneous rocks: A classification and glossary of terms: Cambridge, Cambridge University Press.
Levin, H.L., 2003, The Earth through time: Hoboken, NJ, John Wiley and Sons, 113 p.
Lindsley, D.H., 1991, Experimental studies of oxide minerals, in Lindsley, D.H., ed., Oxide minerals: Petrologic and magnetic significance: Reviews in Mineralogy, v. 25, p. 69–106.
Loomis, T.P., 1982, Numerical simulations of crystallization processes of plagioclase in complex melts: The origin of major and oscillatory zoning in plagioclase: Contributions to Mineralogy and Petrology, v. 81, p. 219–229.
Maniar, P.D., and Piccoli, P.M., 1989, Tectonic discrimination of granitoids: Geological Society of America, Bulletin, v. 101, p. 635–643.
Miller, C.F., and Barton, M.D., 1990, Phanerozoic plutonism in the Cordilleran interior, U.S.A., in Kay, S.M., and Rapela, C.W., eds., Plutonism from Antarctica to Alaska: Geological Society of America Special Paper, v. 241, p. 213–232.
Miller, D., and Hoisch, T., 1992, Mesozoic structure, metamorphism, and magmatism in the Pilot and Toano ranges, *in* Geological Society of America, Rocky Mountain Section Meeting, Field Trip Guide, Ogden, UT, 13–15 May.
Miller, C.F., McDowell, S.M., and Mapes, R.W., 2003, Hot and cold granites? Implications of zircon saturation temperatures and preservation of inheritance: Geology, v. 31, p. 529–532.
Morimoto, N., Fabries, J., Ferguson, A.K., Ginzburg, I.V., Ross, M., Seifert, F.A., Zussman, J., Aoki, K., and Gottardi, G., 1989, Nomenclature of pyroxenes: Canadian Mineralogist, v. 27, p. 143–165.
Pearce, J.A., 1996, Sources and settings of granitic rocks: Episodes, v. 19, p. 120–125.
Pearce, J.A., Harris, N., and Tindle, A.G., 1984, Trace element discrimination diagrams for the tectonic interpretation of granitic rocks: Journal of Petrology, v. 25, p. 956–983.
Pearce, T.H., and Kolisnik, A.M., 1990, Observations of plagioclase zoning using interference imaging: Earth Science Reviews, v. 29, p. 9–26.
Peccerillo, A., and Taylor, S.R., 1976, Geochemistry of Eocene calk-alkaline volcanic rocks from the Kastamonu area, northern Turkey: Contributions to Mineralogy and Petrology, v. 58, p. 63–81.
Petrelli, M., Poli, G., Perugini, D., and Peccerillo, A., 2005, Petrograph: A new software to visualize, model, and present geochemical data in igneous petrology: Geochemistry, Geophysics, and Geosystems, v. 6, Q07011, DOI: 10.1029/2005GC000932.
Piccoli, P., Candela, P., and Rivers, M., 2000, Interpreting magmatic processes from accessory phases: Titanite – a small-scale recorder of large scale processes: Transactions of the Royal Society of Edinburgh, Earth Sciences, v. 91, p. 257–267.
Pitcher, W.S., 1993, The nature and origin of granite: London, Blackie Academic and Professional Publications, 321 p.
Richard, L.R., and Clarke, D.B., 1990, AMPHIBOL: A program for calculating structural formulae and for classifying and plotting chemical analyses of amphiboles: American Mineralogist, v. 75, p. 421–423.
Sanderson, D.D., 1972, Magnetic minerals and properties of the Melrose Stock [Ph.D. thesis]: Michigan State University, 218 p.
Sanderson, D.D., 1974, Spatial distribution and origin of magnetite in an intrusive igneous mass: Geological Society of America Bulletin, v. 85, p. 1183–1188.
Schumacher, J.C., and Czank, M., 1987, Mineralogy of triple- and double-chain pyriboles from Orijärvi, southwest Finland: American Mineralogist, v. 72, p. 345–352.
Shapiro, L., 1975, Rapid analysis of silicate, carbonate and phosphate rocks, revised edition: United States Geological Survey Bulletin, v. 1401, p. 1–54.
Snow, G.G., 1963, Mineralogy and geology of the Dolly Varden Mountains, Elko County, Nevada [Ph.D. thesis]: Salt Lake City, University of Utah, 153 p.
Spencer, K.J., and Lindsley, D.L., 1981, A solution model for coexisting iron–titanium oxides: American Mineralogist, v. 66, p. 1189–1201.
Stormer, J.C., 1975, A practical two-feldspar geothermometer: American Mineralogist, v. 60, p. 667–674.
Stormer, J.C., and Nicholls, J., 1978, XLFRAC: A program for the interactive testing of magmatic differentiation models: Computers and Geosciences, v. 4, p. 143–159.
Suhr, N.H., and Ingamells, C.O., 1966, Solution technique for analysis of silicates: Analytical Chemistry, v. 38, p. 730.
Sun, S., and McDonough, W., 1989, Magmatism in ocean basins: Boston, Blackwell Science.
Tatsumi, Y., and Eggins, S., 1995, Subduction zone magmatism: Boston, Blackwell Science.

Tepley, F.J., Davidson, J.P., and Clynne, M.A., 1999, Magmatic interactions as recorded in plagioclase Phenocrysts of Chaos Crags, Lassen Volcanic Center, California: Journal of Petiology, v. 49, p. 787–806.

Thorman, C., Ketner, K., and Peterson, F., 1992, The Middle to Late Jurassic Elko orogeny in eastern Nevada and western Utah: Geological Society of America, Abstracts with Programs, v. 24, p. 66.

Thornton, C.P., and Tuttle, O.F., 1960, Chemistry of igneous rocks: I – differentiation index: American Journal of Science, v. 258, p. 664–684.

Tindle, A., 2000, MinFormula [online]: The Open University, Available from: http://www.open.ac.uk/earth-research/tindle/AGTWebPages/AGTSoft.html (accessed 16 March 2010).

Watson, E.B., and Harrison, M., 1983. Zircon saturation revisited: Temperature and composition effects in a variety of crustal magma types: Earth and Planetary Science Letters, v. 64, p. 295–304.

Wen, S., and Nekvasil, H., 1994. SOLVCALC: An interactive graphics program package for calculating the ternary feldspar solvus and for two-feldspar geothermometry: Computers and Geosciences, v. 20, p. 1025–1040.

Winter, J.D., 2010, An introduction to igneous and metamorphic petrology: Upper Saddle River, NJ, Pearson Prentice-Hall, Pearson Education Inc., 702 p.

Wones, D.R., 1989, Significance of the assemblage titanite+magnetite+quartz in granitic rocks: American Mineralogist, v. 74, p. 744–749.

Zamudio, J., 1993, Final report for NASA Grant # NAGW-1293, NASA-CR-192091: Boulder, CO, University of Colorado, 5 p.